SANDIA REPORT
SAND2009-1797
Unlimited Release
Printed April 2009

Clutter in the GMTI Range-Velocity Map

Armin W. Doerry

Prepared by
Sandia National Laboratories
Albuquerque, New Mexico 87185 and Livermore, California 94550

Sandia is a multiprogram laboratory operated by Sandia Corporation,
a Lockheed Martin Company, for the United States Department of Energy's
National Nuclear Security Administration under Contract DE-AC04-94AL85000.

Approved for public release; further dissemination unlimited.

Report Documentation Page

Form Approved
OMB No. 0704-0188

Public reporting burden for the collection of information is estimated to average 1 hour per response, including the time for reviewing instructions, searching existing data sources, gathering and maintaining the data needed, and completing and reviewing the collection of information. Send comments regarding this burden estimate or any other aspect of this collection of information, including suggestions for reducing this burden, to Washington Headquarters Services, Directorate for Information Operations and Reports, 1215 Jefferson Davis Highway, Suite 1204, Arlington VA 22202-4302. Respondents should be aware that notwithstanding any other provision of law, no person shall be subject to a penalty for failing to comply with a collection of information if it does not display a currently valid OMB control number.

1. REPORT DATE	2. REPORT TYPE	3. DATES COVERED
APR 2009		**00-00-2009 to 00-00-2009**

4. TITLE AND SUBTITLE	5a. CONTRACT NUMBER
Clutter in the GMTI Range-Velocity Map	5b. GRANT NUMBER
	5c. PROGRAM ELEMENT NUMBER
6. AUTHOR(S)	5d. PROJECT NUMBER
	5e. TASK NUMBER
	5f. WORK UNIT NUMBER
7. PERFORMING ORGANIZATION NAME(S) AND ADDRESS(ES) **Sandia National Laboratories,Albuquerque,NM,87185**	8. PERFORMING ORGANIZATION REPORT NUMBER
9. SPONSORING/MONITORING AGENCY NAME(S) AND ADDRESS(ES)	10. SPONSOR/MONITOR'S ACRONYM(S)
	11. SPONSOR/MONITOR'S REPORT NUMBER(S)

12. DISTRIBUTION/AVAILABILITY STATEMENT
Approved for public release; distribution unlimited

13. SUPPLEMENTARY NOTES

14. ABSTRACT

15. SUBJECT TERMS

16. SECURITY CLASSIFICATION OF:			17. LIMITATION OF ABSTRACT	18. NUMBER OF PAGES	19a. NAME OF RESPONSIBLE PERSON
a. REPORT	b. ABSTRACT	c. THIS PAGE			
unclassified	**unclassified**	**unclassified**	**Same as Report (SAR)**	**60**	

Issued by Sandia National Laboratories, operated for the United States Department of Energy by Sandia Corporation.

NOTICE: This report was prepared as an account of work sponsored by an agency of the United States Government. Neither the United States Government, nor any agency thereof, nor any of their employees, nor any of their contractors, subcontractors, or their employees, make any warranty, express or implied, or assume any legal liability or responsibility for the accuracy, completeness, or usefulness of any information, apparatus, product, or process disclosed, or represent that its use would not infringe privately owned rights. Reference herein to any specific commercial product, process, or service by trade name, trademark, manufacturer, or otherwise, does not necessarily constitute or imply its endorsement, recommendation, or favoring by the United States Government, any agency thereof, or any of their contractors or subcontractors. The views and opinions expressed herein do not necessarily state or reflect those of the United States Government, any agency thereof, or any of their contractors.

Printed in the United States of America. This report has been reproduced directly from the best available copy.

Available to DOE and DOE contractors from

U.S. Department of Energy
Office of Scientific and Technical Information
P.O. Box 62
Oak Ridge, TN 37831

Telephone: (865) 576-8401
Facsimile: (865) 576-5728
E-Mail: reports@adonis.osti.gov
Online ordering: http://www.osti.gov/bridge

Available to the public from

U.S. Department of Commerce
National Technical Information Service
5285 Port Royal Rd.
Springfield, VA 22161

Telephone: (800) 553-6847
Facsimile: (703) 605-6900
E-Mail: orders@ntis.fedworld.gov
Online order: http://www.ntis.gov/help/ordermethods.asp?loc=7-4-0#online

SAND2009-1797
Unlimited Release
Printed April 2009

Clutter in the GMTI Range-Velocity Map

Armin Doerry
SAR Applications Department

Sandia National Laboratories
PO Box 5800
Albuquerque, NM 87185-1330

Abstract

Ground Moving Target Indicator (GMTI) radar maps echo data to range and range-rate, which is a function of a moving target's velocity and its position within the antenna beam footprint. Even stationary clutter will exhibit an apparent motion spectrum and can interfere with moving vehicle detections. Consequently it is very important for a radar to understand how stationary clutter maps into radar measurements of range and velocity. This mapping depends on a wide variety of factors, including details of the radar motion, orientation, and the 3-D topography of the clutter.

Approved for public release; further dissemination unlimited.

Acknowledgements

This report was funded by the Joint DoD/DOE Munitions Program Memorandum of Understanding project.

Thanks to Jeff Hollowell for reviewing an earlier draft of this report and identifying several needed corrections and enhancements.

Contents

Foreword 6
1 Introduction 7
2 The Range-Velocity Map 9
2.1 Moving Target Range 11
2.1.1 Range Difference Expansion 11
2.1.2 Range Resolution 13
2.2 Moving Target Velocity 15
2.2.1 Line-of-Sight Velocity Expansion 15
2.2.2 Velocity Resolution 20
2.3 Clutter in the Range-Doppler Map 21
2.3.1 Flat Terrain in Straight and Level Flight 22
2.3.2 Elevated Terrain in Straight and Level Flight 25
2.3.3 3-D Topography Effects – Range Dependent Topography 27
2.3.4 3-D Topography Effects – Azimuth Dependent Topography 27
2.3.5 Flat Terrain – Radar Vertical Velocity 31
2.4 Antenna Beam Alignment 32
2.4.1 The Antenna Beam Pattern Model 32
2.4.2 The Target Scene Projection Model 35
2.4.3 Target Scene Projection Examples 36
2.5 Clutter Motion 40
2.6 Summary Discussion 41
2.7 Clutter Mitigation 41
3 Conclusions 43
Appendix A – The Phase History Model 45
Reference 59
Distribution 60

Foreword

Recently, questions have arisen over the precise interrelationships of various parameters and characteristics in GMTI radar mode. More recently, new questions have arisen over the impact of target scene topography on GMTI false alarms. The need to account for scene topography is reasonably well-known, and Sandia-designed GMTI systems routinely include provisions to do so. This was discussed to some extent in a section of an earlier limited-release report.[1]

This report details the analytical basis for the GMTI range and velocity measurements, and how clutter is perceived by the GMTI radar.

1 Introduction

Ground Moving Target Indicator (GMTI) radar is a technique whereby a radar measures delay and delay-rate from a sequence of pulses, and infers a moving target's range and velocity from these measurements. However, the transmogrification of the radar measurements into useful range and velocity calculations contains subtleties that may result in errors unless these subtleties are accommodated and the otherwise resulting errors are mitigated.

This requires an appreciation for the finer points of range and Doppler interaction for radar echoes from moving vehicles in various radar and vehicle geometries and motion.

For this report, we will limit ourselves to an exo-clutter GMTI mode, that is, GMTI from a single antenna phase-center.

In the subsequent sections we address a number of issues, including (but not limited to)

- the accuracy of a target velocity measurement,
- the location and shape of clutter in the range-Doppler map,
- the effects of antenna rotation on target scene illumination, and
- the effects of target area topography on velocity measurements.

Examples are given to illustrate these issues.

Clutter

A reasonable question is "Why is the location/shape of the clutter band important?"

First, the width of the clutter band in velocity-space defines the Minimum Detectable Velocity (MDV) for an exo-clutter GMTI radar. Things that cause the clutter band to widen or narrow, also cause the MDV to change.

Second, the clutter band denotes a 'stay-out' region where otherwise clutter is expected to generate an unacceptable degree of false alarm detections. As the clutter-band moves, so too should the stay-out region.

Third, the location of the center of the antenna beam footprint in velocity-space defines the reference velocity for any moving target, that is, the difference between this velocity and the raw measured velocity of a target detection represents the best estimate of the target's own range-rate. As the center of the beam moves in velocity-space, so too does the reference velocity.

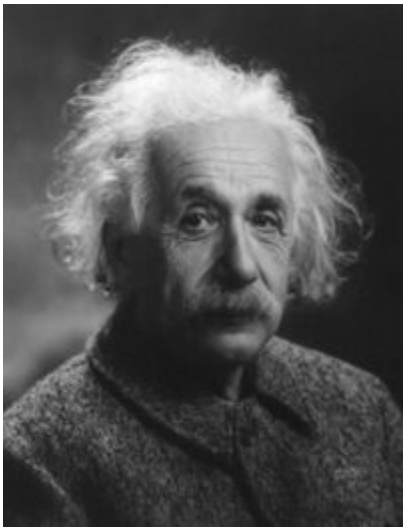

"Nothing happens until something moves."
— Albert Einstein

2 The Range-Velocity Map

A model for the video phase history data for a stretch-processed[2] GMTI Coherent Processing Interval (CPI) is derived in Appendix A. It is expressed as

$$X_V(i,n) = A_r \exp\left\{ j \left(\begin{array}{l} -\frac{2\gamma_{T,0}}{c}(1-\zeta_0)(r_{s,0,0} - r_{c,0,0})T_s i \\ -\frac{2\omega_{T,0}}{c}(v_{los,s,0,0} - v_{los,c,0,0})T_p n \\ +\frac{4\gamma_{T,0}}{c^2}(r_{s,0,0} - r_{c,0,0})(v_{los,s,0,0} - v_{los,c,0,0})T_p n \end{array} \right) \right\}. \quad (1)$$

where

$$(v_{los,s,0,0} - v_{los,c,0,0}) = \left(\frac{\mathbf{r}_s(t_0 + t_{c,0,0})}{|\mathbf{r}_s(t_0 + t_{c,0,0})|} - \frac{\mathbf{r}_c(t_0 + t_{c,0,0})}{|\mathbf{r}_c(t_0 + t_{c,0,0})|} \right) \bullet \mathbf{v}_c - v_{los,t,0,0} \quad (2)$$

and individual parameters are identified as

i = the index for ADC samples of a single pulse's echo data,
n = the pulse index within a CPI,
A_r = the target's echo strength.
$\omega_{T,0}$ = the transmitted reference radian frequency,
$\gamma_{T,0}$ = the transmitted reference radian chirp rate,
ζ_n = a factor that depends on line-of-sight velocity (see Appendix A),
$\mathbf{r}_s(t)$ = the vector difference between radar location and target location,
$\mathbf{r}_c(t)$ = the vector location of the radar with respect to the SRP,
$r_{s,n,i}$ = the nominal range between radar and target,
$r_{c,n,i}$ = the nominal range between radar and SRP,
$\mathbf{v}_c$ = the radar velocity vector,
$v_{los,s,n,i}$ = the nominal line-of-sight velocity between radar and target,
$v_{los,c,n,i}$ = the nominal line-of-sight velocity between radar and SRP,
$v_{los,t,n,i}$ = the nominal line-of-sight velocity component of just the target,
T_s = the ADC sampling period,
T_p = the pulse period, and
c = the velocity of propagation. (3)

A more complete description of these parameters can be found in Appendix A.

The Scene Reference Point (SRP) is the location at which the antenna is pointed, and to which any motion compensation is referenced. It defines zero range offset, and zero Doppler offset at that range.

The third phase term is a consequence of the Residual Video Phase Error (RVPE) term resulting from stretch processing (deramping the chirp upon receive). It is typically ignored for GMTI applications, and we shall do so hereafter.

In the first phase term, to simplify the following discussion, we define the range difference

$$r_{sc} = \left(r_{s,0,0} - r_{c,0,0}\right). \tag{4}$$

In the second phase term, to simplify the following discussion, we define the line-of-sight velocity difference

$$v_{los,sc} = \left(v_{los,s,0,0} - v_{los,c,0,0}\right). \tag{5}$$

The model then becomes

$$X_V(i,n) = A_r \exp\left\{ j \begin{pmatrix} -\frac{2\gamma_{T,0}}{c}(1-\zeta_0) r_{sc} T_s i \\ -\frac{2\omega_{T,0}}{c} v_{los,sc} T_p n \end{pmatrix} \right\}. \tag{6}$$

An examination of the model for the video phase history data shows that the phase is a function of the two data indices *n* and *i*.

A Discrete Fourier Transforms (DFT) across index *n* will then yield an Impulse Response (IPR) with peak at apparent velocity offset

$$v_{peak} = v_{los,sc} \tag{7}$$

A DFT across index *i* will yield an IPR with peak at apparent range offset

$$r_{peak} = (1-\zeta_0) r_{sc} \tag{8}$$

We now examine these in turn.

2.1 Moving Target Range

2.1.1 Range Difference Expansion

The entity of concern is $(1-\zeta_0)r_{sc}$. From Appendix A, we recall that the factor ζ_0 is given by

$$\zeta_0 = \begin{cases} \frac{2}{c}\left(v_{los,s,0,0} - v_{los,c,0,0}\right) & \text{if we modulate } \gamma_{T,n} \\ \frac{2}{c} v_{los,s,0,0} & \text{if we don't} \end{cases}. \tag{9}$$

For all reasonable velocities of interest,

$$v_{los,s,0,0} << c\,. \tag{10}$$

Consequently, while perhaps important for focusing a Synthetic Aperture Radar (SAR) image, we may presume that ζ_0 has negligible consequence for scaling r_{sc} in a typical GMTI mode. That is, we will presume

$$(1-\zeta_0)r_{sc} \approx r_{sc}\,.$$

We identify the range difference as

$$r_{sc} = \left(r_{s,0,0} - r_{c,0,0}\right) = \left|\mathbf{r}_s\left(t_0 + t_{c,0,0}\right)\right| - \left|\mathbf{r}_c\left(t_0 + t_{c,0,0}\right)\right|. \tag{11}$$

We make use of the following equivalence

$$\mathbf{r}_s\left(t_0 + t_{c,0,0}\right) = \mathbf{r}_c\left(t_0 + t_{c,0,0}\right) - \mathbf{s}_0\left(t_0 + t_{c,0,0}\right). \tag{12}$$

For convenience and clarity, we recognize that these are constant values with time, and therefore dispense with the overt time arguments. Consequently we now write this as

$$\mathbf{r}_s = \mathbf{r}_c - \mathbf{s}_0\,. \tag{13}$$

We note that

$$\left|\mathbf{r}_s\right| = \left|\mathbf{r}_c - \mathbf{s}_0\right| = \sqrt{\left(\mathbf{r}_c - \mathbf{s}_0\right)\bullet\left(\mathbf{r}_c - \mathbf{s}_0\right)} = \left|\mathbf{r}_c\right|\sqrt{1 + \frac{\left|\mathbf{s}_0\right|^2}{\left|\mathbf{r}_c\right|^2} - \frac{2\mathbf{r}_c \bullet \mathbf{s}_0}{\left|\mathbf{r}_c\right|^2}} \tag{14}$$

which allows

$$r_{sc} = |\mathbf{r}_c| \left(\sqrt{1 + \frac{|\mathbf{s}_0|^2}{|\mathbf{r}_c|^2} - \frac{2\mathbf{r}_c \bullet \mathbf{s}_0}{|\mathbf{r}_c|^2}} - 1 \right). \tag{15}$$

For a number of SAR image formation algorithms (e.g. Polar Format processing[3,4]), we use the Taylor series expansion

$$\sqrt{1+a} \approx 1 + \frac{a}{2} - \frac{a^2}{8} + \frac{a^3}{16} + \ldots . \tag{16}$$

and then often only the linear term. Doing so allows the approximation

$$r_{sc} \approx \frac{|\mathbf{s}_0|^2}{2|\mathbf{r}_c|} - \frac{\mathbf{r}_c \bullet \mathbf{s}_0}{|\mathbf{r}_c|}. \tag{17}$$

This is only really well approximated for $r_{sc} << |\mathbf{r}_c|$. While often valid for SAR, it is less tractable for the large swaths of a wide-area search GMTI mode.

Nevertheless, even near the center of the range swath, for the region where in fact $r_{sc} << |\mathbf{r}_c|$, we will observe behavior that is of interest to us. Consequently we will proceed with the simplified approximation for r_{sc} simply to gain some insight to the phenomenon.

We identify the target coordinates as

$$\mathbf{s}_0 = s_x \hat{x} + s_y \hat{y} + s_z \hat{z} \tag{18}$$

where $\hat{x}, \hat{y}, \hat{z}$ identify orthogonal unit vectors. We identify the radar coordinates as

$$\mathbf{r}_c = -r_c \cos\psi_0 \hat{y} + r_c \sin\psi_0 \hat{z} \tag{19}$$

where

r_c = nominal scalar range between radar and scene center, and
ψ_0 = nominal grazing angle at scene center. (20)

Consequently, we may simplify

$$r_{sc} \approx \cos\psi_0 s_y - \sin\psi_0 s_z + \left(s_x{}^2 + s_y{}^2 + s_z{}^2\right)\Big/ 2r_c \ . \tag{21}$$

At this point we make some observations.

- The radar measures $(1-\zeta_0)r_{sc}$. In general, r_{sc} depends on exclusively target location. There is a minor dependence in what the radar measures via ζ_0, but this is a very minor factor.
- In general, r_{sc} depends on offsets from the SRP in all three dimensions, namely all components s_x, s_y, s_z. However the dominant dependence is on the components s_y, s_z.
- Dependence of r_{sc} on target height increases as the grazing angle increases. This is the familiar range-layover, or foreshortening, effect.

To first order, we can often simplify the range difference model even more to

$$(1-\zeta_0)r_{sc} \approx -\frac{\mathbf{r}_c \bullet \mathbf{s}_0}{|\mathbf{r}_c|} = \cos\psi_0 s_y - \sin\psi_0 s_z \ . \tag{22}$$

The fidelity of the various range models are illustrated in Figure 1.

2.1.2 Range Resolution

The resolution with which we can measure range is given by setting

$$\frac{2\gamma_{T,0}}{c}(1-\zeta_0)r_{sc}T_s i\Big|_{\substack{i=I \\ r_{sc}=\rho_r}} = 2\pi \tag{23}$$

where

$$\rho_r = \text{[slant] range resolution.} \tag{24}$$

This is solved to yield

$$\rho_r = \frac{2\pi c}{(1-\zeta_0)T_s I 2\gamma_{T,0}} = \frac{c}{(1-\zeta_0)2B_{eff}} \tag{25}$$

where

$$B_{eff} = \frac{T_s I \gamma_{T,0}}{2\pi} = \text{the nominal effective bandwidth in Hz contained within the data.} \tag{26}$$

The effective bandwidth B_{eff} is often very nearly the actual transmitted bandwidth, but may be less, especially if pulses are short compared to the range swath being processed.

Very typically $\zeta_0 << 1$, so it is often ignored. This implies that an adequate expression for range resolution is

$$\rho_r = \frac{c}{2B_{eff}}. \tag{27}$$

Note that this is the achievable resolution of the system, and does not account for any coarsening due to sidelobe filtering such as with window functions prior to the range compression (the DFT across index *i*).

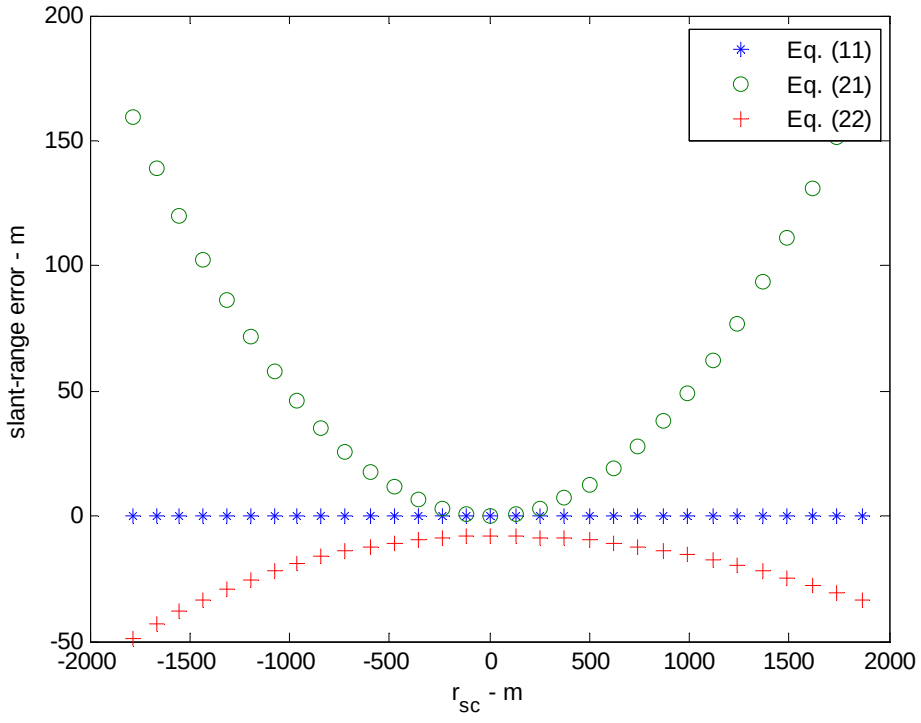

Figure 1. Example slant range error of various models for r_{sc}. Swath was 4 km on the ground at 10 km center slant range from 4 km altitude, with 400 m azimuth offset.

2.2 Moving Target Velocity

2.2.1 Line-of-Sight Velocity Expansion

We now investigate the term

$$v_{los,sc} = \left(v_{los,s,0,0} - v_{los,c,0,0}\right) = \left(\frac{\mathbf{r}_s\left(t_0 + t_{c,0,0}\right)}{\left|\mathbf{r}_s\left(t_0 + t_{c,0,0}\right)\right|} - \frac{\mathbf{r}_c\left(t_0 + t_{c,0,0}\right)}{\left|\mathbf{r}_c\left(t_0 + t_{c,0,0}\right)\right|} \right) \bullet \mathbf{v}_c - v_{los,t,0,0} \,. \tag{28}$$

As with the range analysis, we make use of the following equivalence

$$\mathbf{r}_s\left(t_0 + t_{c,0,0}\right) = \mathbf{r}_c\left(t_0 + t_{c,0,0}\right) - \mathbf{s}_0\left(t_0 + t_{c,0,0}\right) \tag{29}$$

and for convenience and clarity, write this as

$$\mathbf{r}_s = \mathbf{r}_c - \mathbf{s}_0 \,. \tag{30}$$

Furthermore, we recall that

$$r_{sc} = \left|\mathbf{r}_s\right| - \left|\mathbf{r}_c\right| \,. \tag{31}$$

This allows the expansion in terms of just the radar geometry and the target geometry as

$$v_{los,sc} = \left(\frac{\left|\mathbf{r}_c\right|}{\left|\mathbf{r}_c\right| + r_{sc}} - 1 \right) \frac{\mathbf{r}_c \bullet \mathbf{v}_c}{\left|\mathbf{r}_c\right|} - \frac{\mathbf{s}_0 \bullet \mathbf{v}_c}{\left|\mathbf{r}_c\right| + r_{sc}} - v_{los,t,0,0} \tag{32}$$

which can be rearranged to the somewhat more convenient form for our purposes

$$v_{los,sc} = \left(\frac{1}{1 + \frac{r_{sc}}{\left|\mathbf{r}_c\right|}} - 1 \right) \frac{\mathbf{r}_c \bullet \mathbf{v}_c}{\left|\mathbf{r}_c\right|} - \left(\frac{1}{1 + \frac{r_{sc}}{\left|\mathbf{r}_c\right|}} \right) \frac{\mathbf{s}_0 \bullet \mathbf{v}_c}{\left|\mathbf{r}_c\right|} - v_{los,t,0,0} \,. \tag{33}$$

Note that we can employ the Taylor series expansion

$$\frac{1}{1+a} = 1 - a + a^2 - a^3 + a^4 + ... = \sum_n (-a)^n \qquad \text{for } |a| < 1, \text{ and } n \geq 0 \,. \tag{34}$$

The number of terms required for high fidelity depends on just how much $|a| < 1$.

In any case, this allows the rearrangement to

$$v_{los,sc} = \left(\sum_n \left(-\frac{r_{sc}}{|\mathbf{r}_c|} \right)^n - 1 \right) \frac{\mathbf{r}_c \bullet \mathbf{v}_c}{|\mathbf{r}_c|} - \left(\sum_n \left(-\frac{r_{sc}}{|\mathbf{r}_c|} \right)^n \right) \frac{\mathbf{s}_0 \bullet \mathbf{v}_c}{|\mathbf{r}_c|} - v_{los,t,0,0} \cdot \tag{35}$$

The relationship of r_{sc} to $\mathbf{s}_0$ was explored in the previous section. Recall that the radar in fact measures r_{sc}.

While for wide-area search modes we may often have large range swaths compared to the center range, it remains instructive to examine the region near the center of the swath, where $r_{sc} << |\mathbf{r}_c|$. In this region, the model for line-of-sight velocity can be approximated as

$$v_{los,sc} = -\left(\frac{r_{sc}}{|\mathbf{r}_c|} \right) \frac{\mathbf{r}_c \bullet \mathbf{v}_c}{|\mathbf{r}_c|} - \frac{\mathbf{s}_0 \bullet \mathbf{v}_c}{|\mathbf{r}_c|} - v_{los,t,0,0} \cdot \tag{36}$$

This can be expanded to

$$v_{los,sc} = -\left(\frac{|\mathbf{s}_0|^2}{2|\mathbf{r}_c|^2} - \frac{\mathbf{r}_c \bullet \mathbf{s}_0}{|\mathbf{r}_c|^2} \right) \frac{\mathbf{r}_c \bullet \mathbf{v}_c}{|\mathbf{r}_c|} - \frac{\mathbf{s}_0 \bullet \mathbf{v}_c}{|\mathbf{r}_c|} - v_{los,t,0,0} \cdot \tag{37}$$

At this point, to gain further insight, we need to pick a coordinate frame, and constrain the flight path.

We shall continue with target coordinates and radar coordinates as previously defined. Accordingly, we identify the radar velocity vector as

$$\mathbf{v}_c = -v_a \sin\theta_s \hat{x} + v_a \cos\theta_s \hat{y} + v_z \hat{z} \tag{38}$$

where

v_a = horizontal (with respect to target plane) radar velocity magnitude,
v_z = vertical radar velocity,
θ_s = squint angle as projected into target plane. (39)

We will use the convention for squint angle as depicted in Figure 2. This accounts for the negative sign in front of the $\hat{x}$ component in the radar velocity vector.

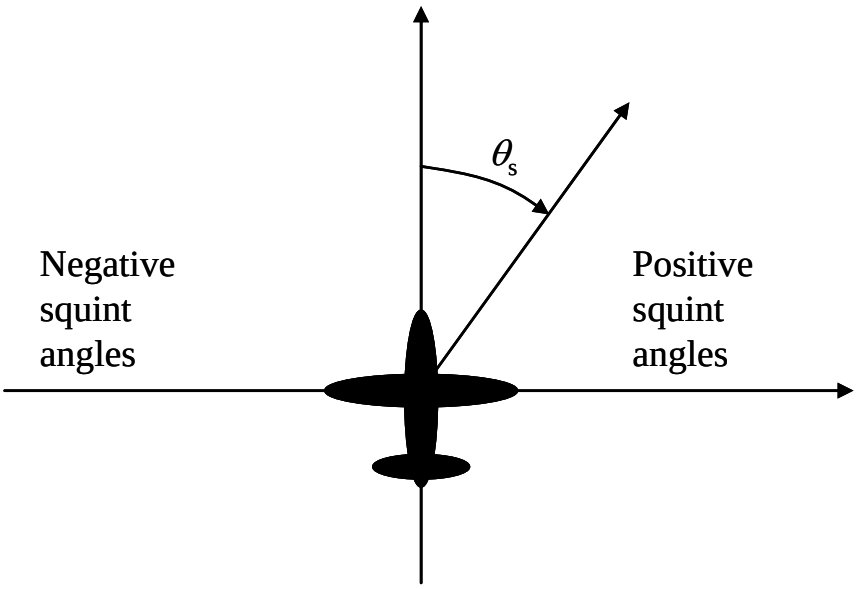

Figure 2. Convention for squint angle.

Putting all this together yields the expansion

$$v_{los,sc} = \left(\begin{array}{l} \dfrac{v_a \sin\theta_s s_x}{|\mathbf{r}_c|} - \dfrac{v_a \cos\psi_0 \cos\theta_s s_x^{\,2}}{2|\mathbf{r}_c|^2} - \dfrac{v_z \sin\psi_0 s_x^{\,2}}{2|\mathbf{r}_c|^2} \\ - \dfrac{v_a \sin^2\psi_0 \cos\theta_s s_y}{|\mathbf{r}_c|} - \dfrac{v_a \cos\psi_0 \cos\theta_s s_y^{\,2}}{2|\mathbf{r}_c|^2} \\ + \dfrac{v_z \cos\psi_0 \sin\psi_0 s_y}{|\mathbf{r}_c|} - \dfrac{v_z \sin\psi_0 s_y^{\,2}}{2|\mathbf{r}_c|^2} \\ + \dfrac{v_a \cos\psi_0 \cos\theta_s \sin\psi_0 s_z}{|\mathbf{r}_c|} - \dfrac{v_a \cos\psi_0 \cos\theta_s s_z^{\,2}}{2|\mathbf{r}_c|^2} \\ - \dfrac{v_z s_z \cos^2\psi_0}{|\mathbf{r}_c|} - \dfrac{v_z \sin\psi_0 s_z^{\,2}}{2|\mathbf{r}_c|^2} \\ - v_{los,t,0,0} \end{array} \right). \qquad (40)$$

If we insist on straight and level flight ($v_z = 0$), then this reduces to

$$v_{los,sc} = \begin{pmatrix} \dfrac{v_a \sin\theta_s s_x}{|\mathbf{r}_c|} - \dfrac{v_a \cos\psi_0 \cos\theta_s {s_x}^2}{2|\mathbf{r}_c|^2} \\ - \dfrac{v_a \sin^2\psi_0 \cos\theta_s s_y}{|\mathbf{r}_c|} - \dfrac{v_a \cos\psi_0 \cos\theta_s {s_y}^2}{2|\mathbf{r}_c|^2} \\ + \dfrac{v_a \cos\psi_0 \cos\theta_s \sin\psi_0 s_z}{|\mathbf{r}_c|} - \dfrac{v_a \cos\psi_0 \cos\theta_s {s_z}^2}{2|\mathbf{r}_c|^2} \\ - v_{los,t,0,0} \end{pmatrix}. \tag{41}$$

By reducing our model even further, by neglecting the $|\mathbf{r}_c|^{-2}$ terms, we arrive at

$$v_{los,sc} = \begin{pmatrix} \dfrac{v_a \sin\theta_s s_x}{|\mathbf{r}_c|} - \dfrac{v_a \sin^2\psi_0 \cos\theta_s s_y}{|\mathbf{r}_c|} \\ + \dfrac{v_a \cos\psi_0 \cos\theta_s \sin\psi_0 s_z}{|\mathbf{r}_c|} \\ - v_{los,t,0,0} \end{pmatrix}. \tag{42}$$

At this point we make some observations.

- The radar measures $v_{los,sc}$.
- In general, $v_{los,sc}$ depends on both the target velocity, and the target location.
- In general, $v_{los,sc}$ depends on offsets from the SRP in all three dimensions, namely all components s_x, s_y, s_z.
- Dependence of $v_{los,sc}$ on target height increases as the squint angle approaches zero, that is, as the radar operates towards the direction of the velocity vector of the radar.

Remember that this model is only really valid near the center of the range swath. However, we do expect that the dependencies on geometry will not lessen appreciably as distance from swath center increases.

Target Height Equivalent Azimuth Shift

An important question is "How sensitive is the apparent clutter velocity to target scene height?"

We answer this by relating line-of-sight velocity due to stationary target height, to line-of-sight velocity due to stationary target azimuth offset. That is, we set

$$\frac{v_a \sin\theta_s s_x}{|\mathbf{r}_c|} = \frac{v_a \cos\psi_0 \cos\theta_s \sin\psi_0 s_z}{|\mathbf{r}_c|} . \tag{43}$$

Solving this yields

$$s_x = \left(\frac{1}{2}\sin(2\psi_0)\cot\theta_s\right) s_z . \tag{44}$$

Note that this is dependent on both squint and grazing angles. This is plotted in Figure 3. Note that at small angles, the relationship can be much more than one-to-one. That is, a target height can sometimes be equivalent to an even greater target azimuth offset.

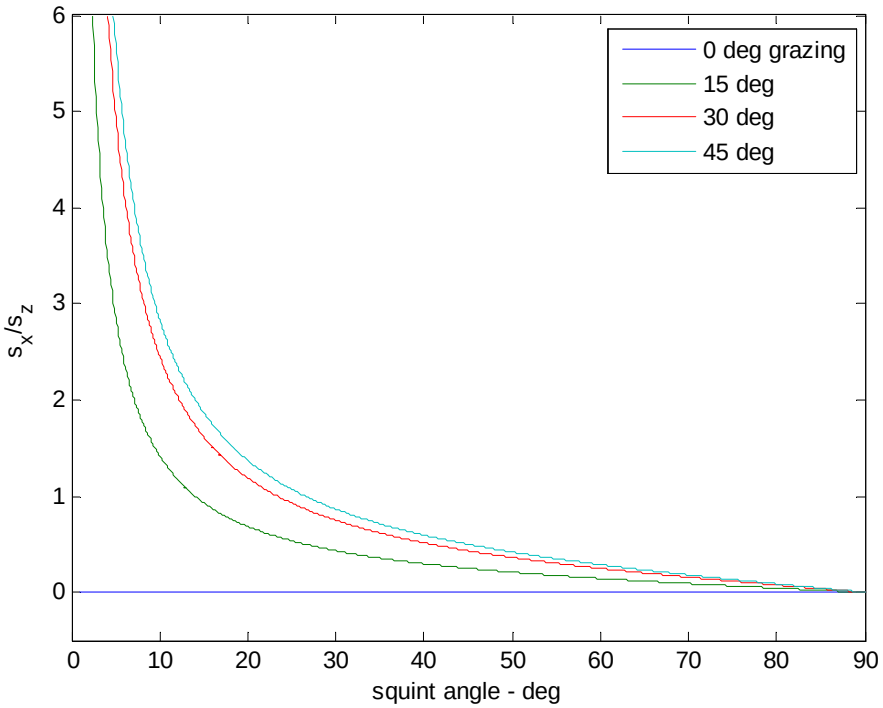

Figure 3. Apparent azimuth shift due to target height as a function of squint angle, for various grazing angles.

2.2.2 Velocity Resolution

The resolution with which we can measure velocity is given by setting

$$\frac{2\omega_{T,0}}{c} v_{los,sc} T_p n \Big|_{\substack{n=N \\ v_{los,sc}=\rho_v}} = 2\pi \tag{45}$$

where

ρ_v = velocity resolution. (46)

This is solved to yield

$$\rho_v = \frac{2\pi c}{T_p N 2\omega_{T,0}} = \frac{\lambda_0}{2NT_p} \tag{47}$$

where

$\lambda_0 = \frac{2\pi c}{\omega_{T,0}}$ = the nominal transmitted wavelength. (48)

We note that NT_p is the total collection time, that is, the duration of the CPI. Note also that this is the achievable resolution of the system, and does not account for any coarsening due to sidelobe filtering such as with window functions prior to the velocity compression (the DFT across index *n*).

Example

Consider a GMTI radar that operates with the following parameters.

λ_0 = 0.018 m (Ku-band),
N = 256 pulses,
T_p = 250 μs (PRF = 4 kHz). (49)

These parameters allow a velocity resolution of

ρ_v = 0.14 m/s. (50)

Note that the velocity *resolution* is independent of radar velocity. We do note that in SAR, sometimes PRF is slaved to velocity, making velocity resolution dependent on velocity in this case. However, this is generally not true for GMTI.

2.3 Clutter in the Range-Doppler Map

We are concerned here with the Doppler signatures of stationary clutter. Of course Doppler yields a measure of relative velocity. So we limit our attention to $v_{los,sc}$ when $v_{los,t,0,0} = 0$.

Clutter generally provides an area of target echo responses. The only limitation is the illumination provided by the antenna beam itself. Consequently, the antenna provides to the radar echo soundings from a specific region, where that region offers a spread of velocity indications.

Clearly, the nature of the spread of velocity indications is defined by the antenna beam shape and orientation. That is, Doppler bandwidth, and hence the velocity spread, is limited by the antenna beamwidth, primarily the azimuth beamwidth.

For a typical elliptical antenna beam pattern, the illuminated region on the ground will also be elliptical in nature, with a larger region illuminated down-range from the boresight than from ranges closer than the boresight. Examples will be given in later sections of this report.

We begin by returning to the exact models for range and velocity, namely

$$r_{sc} = |\mathbf{r}_c| \left(\sqrt{1 + \frac{|\mathbf{s}_0|^2}{|\mathbf{r}_c|^2} - \frac{2\mathbf{r}_c \bullet \mathbf{s}_0}{|\mathbf{r}_c|^2}} - 1 \right), \text{ and}$$

$$v_{los,sc} = \left(\frac{1}{1 + \frac{r_{sc}}{|\mathbf{r}_c|}} - 1 \right) \frac{\mathbf{r}_c \bullet \mathbf{v}_c}{|\mathbf{r}_c|} - \left(\frac{1}{1 + \frac{r_{sc}}{|\mathbf{r}_c|}} \right) \frac{\mathbf{s}_0 \bullet \mathbf{v}_c}{|\mathbf{r}_c|} - v_{los,t,0,0}. \tag{51}$$

Recall that vector quantities are defined as

$$\begin{aligned} \mathbf{s}_0 &= s_x \hat{x} + s_y \hat{y} + s_z \hat{z}, \\ \mathbf{r}_c &= -r_c \cos\psi_0 \hat{y} + r_c \sin\psi_0 \hat{z}, \text{ and} \\ \mathbf{v}_c &= -v_a \sin\theta_s \hat{x} + v_a \cos\theta_s \hat{y} + v_z \hat{z}. \end{aligned} \tag{52}$$

Consequently, we calculate the various dot products as

$$\mathbf{r}_c \bullet \mathbf{s}_0 = -r_c \cos\psi_0 s_y + r_c \sin\psi_0 s_z ,$$
$$\mathbf{r}_c \bullet \mathbf{v}_c = -v_a r_c \cos\psi_0 \cos\theta_s + v_z r_c \sin\psi_0 , \text{ and}$$
$$\mathbf{s}_0 \bullet \mathbf{v}_c = -v_a \sin\theta_s s_x + v_a \cos\theta_s s_y + v_z s_z . \quad (53)$$

Since GMTI processing nearly always involves first processing a range-Doppler map, and Doppler is proportional to line-of-sight velocity, we are interested in how clutter maps onto a grid of r_{sc} versus $v_{los,sc}$.

To simplify the analysis, and to make some specific points, we will confine our interest to a rectangular scene of interest, oriented in $\hat{x}$ and $\hat{y}$ directions. We note that the illuminated region of clutter will generally not be a rectangle, as previously discussed. Nevertheless, we will proceed with the rectangular scene of interest and observe that the effects within the rectangular scene of interest will apply also to regions outside the rectangular scene of interest.

For the following examples, unless noted otherwise, we will assume the following parameters

v_a = 100 m/s,
$|\mathbf{r}_c|$ = 10 km,
ψ_0 = 30 degrees. (54)

2.3.1 Flat Terrain in Straight and Level Flight

We first consider a flat target plane with $s_z = 0$. Straight and level flight implies $v_z = 0$.

Example

Consider a target scene with stationary reflectors arranged with ground truth as in Figure 4. Now consider the scene being interrogated from a number of different squint angles. The resulting range-velocity maps are depicted for squint angles of –90, –60, and –30 degrees respectively in Figure 5, Figure 6, and Figure 7.

We observe the following.

- Except at broadside squint angles, there is a range-dependent shift in apparent clutter velocity. It is non-linear with range, and manifests as a ‘comma’ shape.
- The scene’s velocity band narrows in velocity as squint angle moves away from broadside.

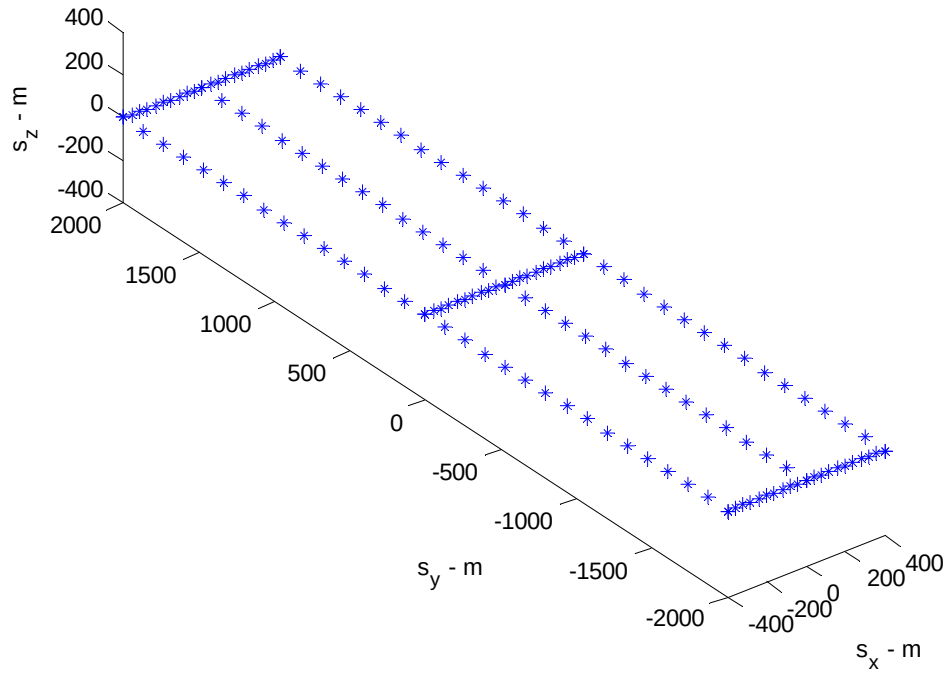

Figure 4. Example ground truth for stationary reflectors.

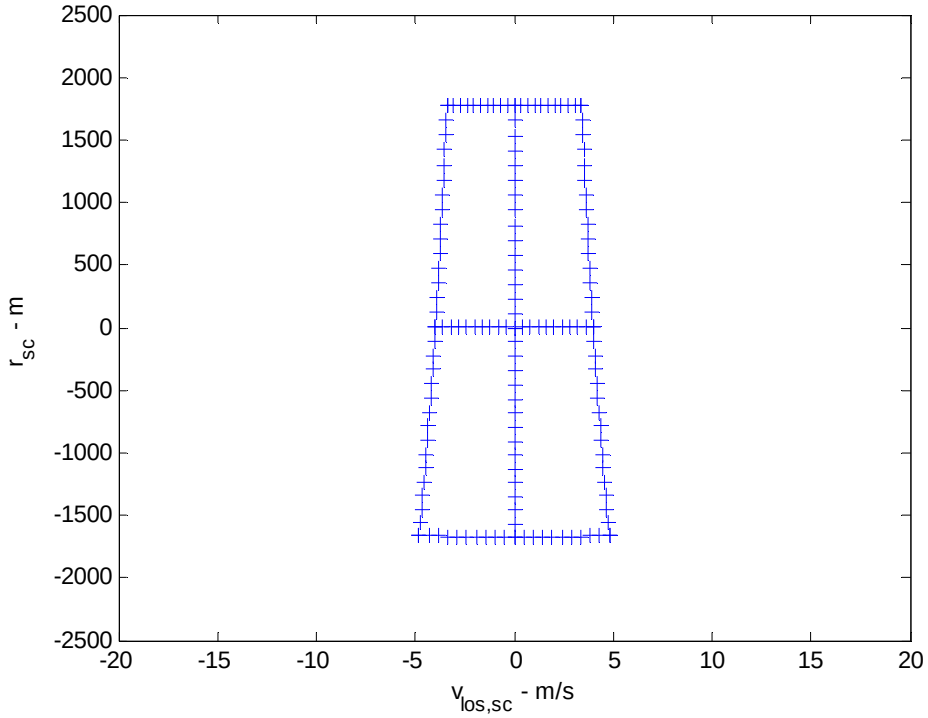

Figure 5. Range- velocity map for -90 degree squint angle.

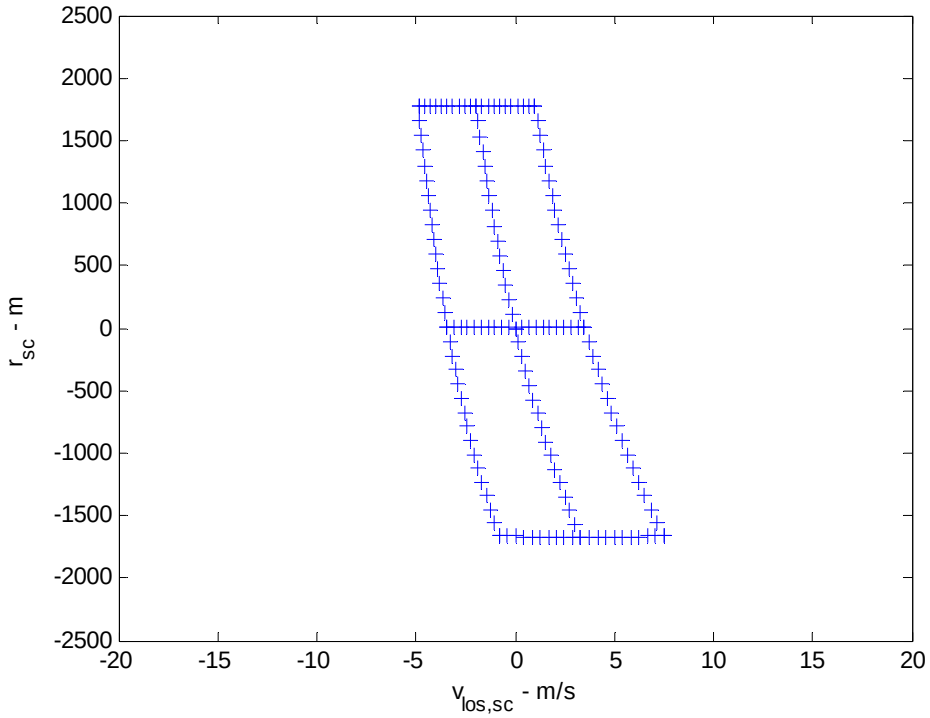

Figure 6. Range- velocity map for -60 degree squint angle.

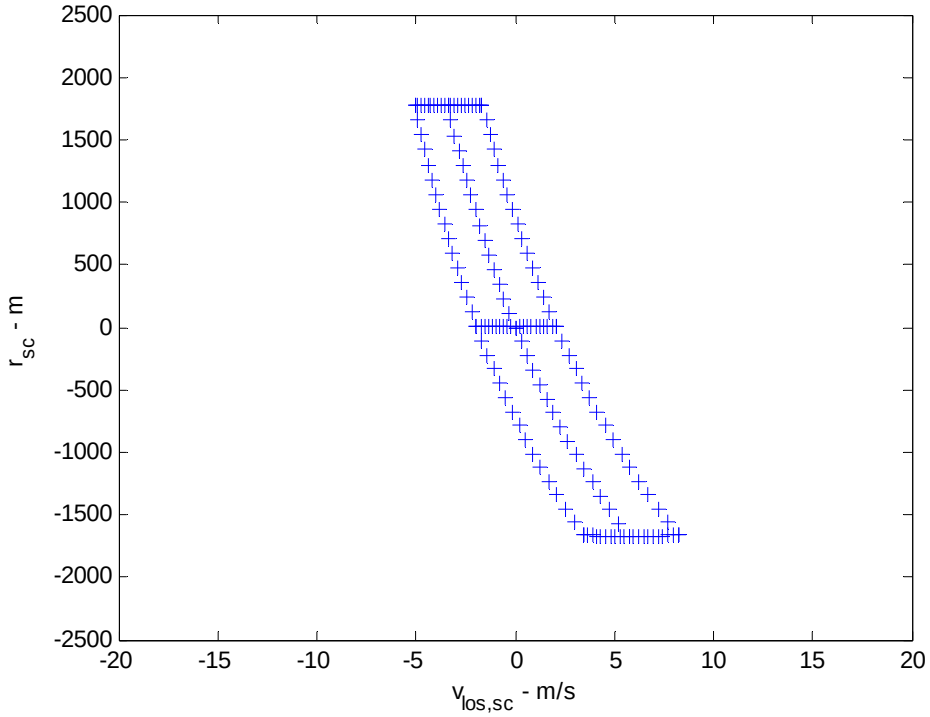

Figure 7. Range- velocity map for -30 degree squint angle.

2.3.2 Elevated Terrain in Straight and Level Flight

We now concern ourselves with the condition $s_z \neq 0$.

Example

With respect to the previous example, we now raise the target plane by 200 m. Otherwise it remains flat. Now consider the scene being interrogated from the same squint angles as those of the previous examples. The resulting range-velocity maps are depicted for squint angles of –90, –60, and –30 degrees respectively in Figure 8, Figure 9, and Figure 10.

This exhibited shifting is 'layover' in SAR images, and happens in both range and velocity, depending on geometry. As a sanity check, we note that on the left side of the flight path, and forward of broadside, as the stationary target is elevated, it achieves a smaller angle with respect to the velocity vector, hence exhibits a more positive closing-rate, and hence a more negative range-rate, that is, a more negative line-of-sight velocity. It also exhibits a closer range. Hey, it checks out…

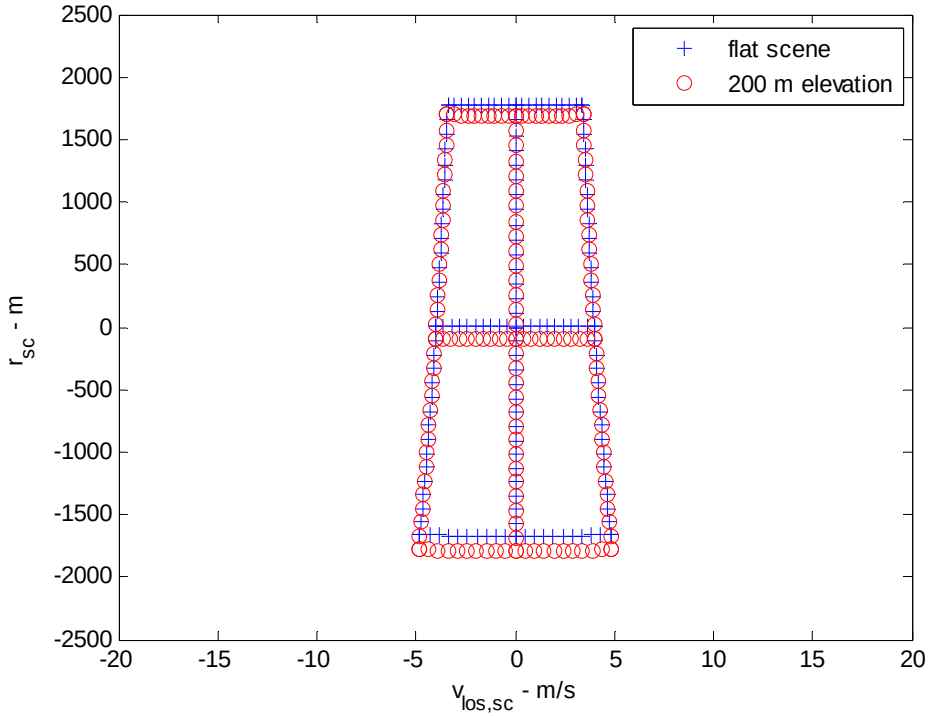

Figure 8. Range- velocity map for -90 degree squint angle.

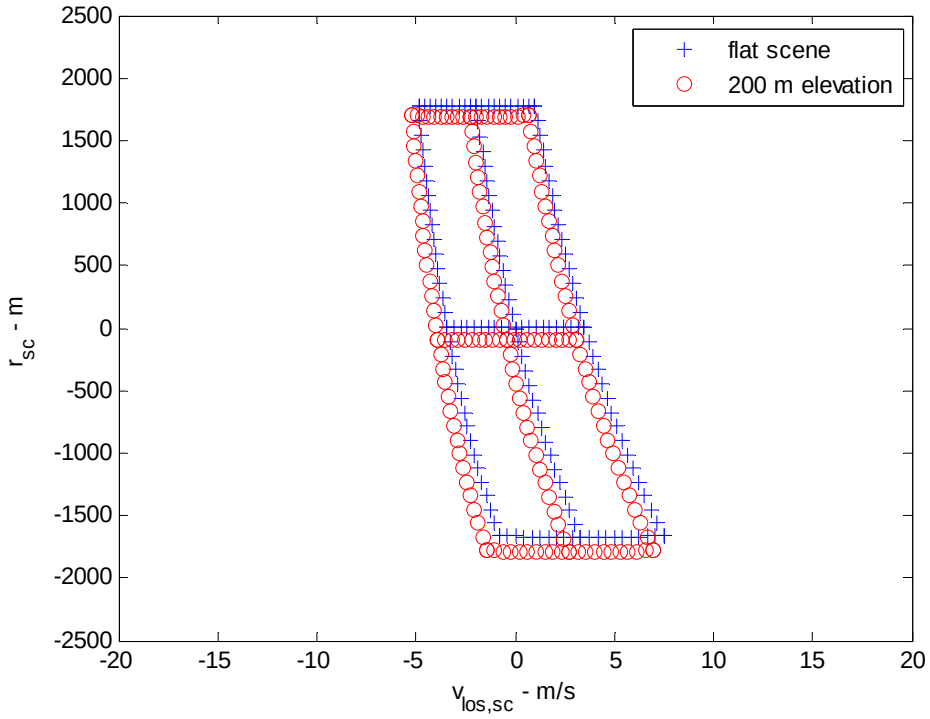

Figure 9. Range- velocity map for -60 degree squint angle.

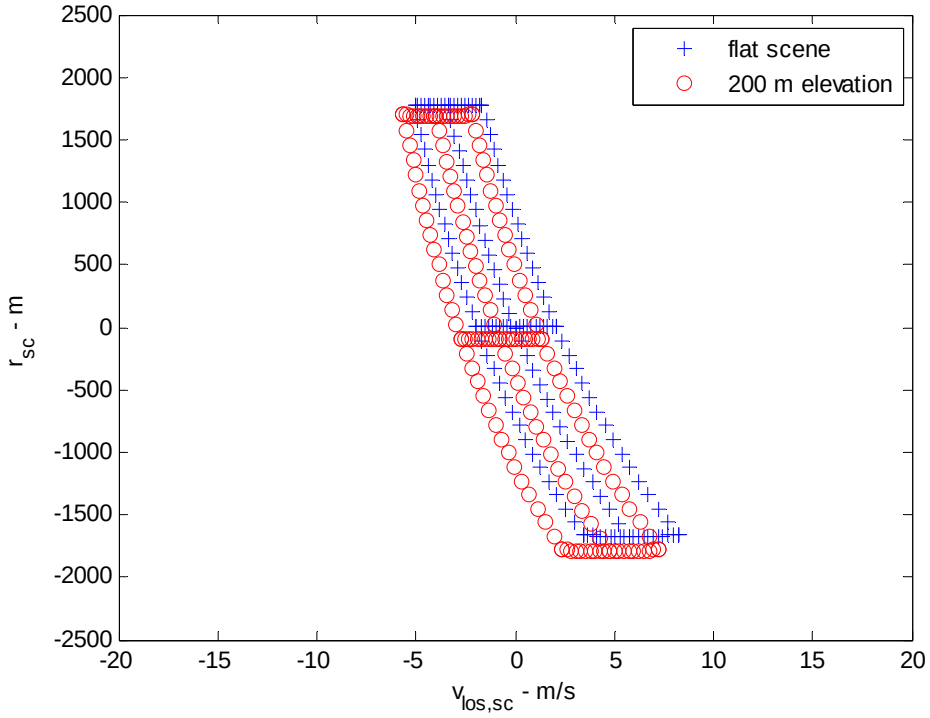

Figure 10. Range- velocity map for -30 degree squint angle.

2.3.3 3-D Topography Effects – Range Dependent Topography

We now concern ourselves with the condition $s_z \neq 0$, where elevation varies with range. The radar is still presumed to fly straight and level.

Example

Now consider a target scene with stationary reflectors arranged with ground truth that includes height topography as in Figure 11. Now consider the scene being interrogated from a number of different squint angles matching those of the previous examples. The resulting range-velocity maps are depicted for squint angles of –90, –60, and –30 degrees respectively in Figure 12, Figure 13, and Figure 14.

We observe the following.

- Variations in target height will cause variations in apparent target velocity.
- An elevation offset that is constant at any one range will cause a shift in the scene's velocity band.
- The degree of target-height induced velocity variations depends on the squint angle, increasing as the viewing geometry moves away from broadside.

2.3.4 3-D Topography Effects – Azimuth Dependent Topography

In the previous section, we concerned ourselves with a range-dependent clutter elevation variation. We now concern ourselves with an azimuth-dependent elevation variation of the clutter. The radar is still presumed to fly straight and level.

Example

Consider the same GMTI radar as in the previous examples. Now consider a target scene with stationary reflectors arranged with ground truth that includes height topography as in Figure 15. Figure 16 illustrates the range-Doppler map when interrogated at a –30 degree squint angle.

We observe that the scene's velocity band has widened.

With other slopes, the scene's velocity band may in fact narrow.

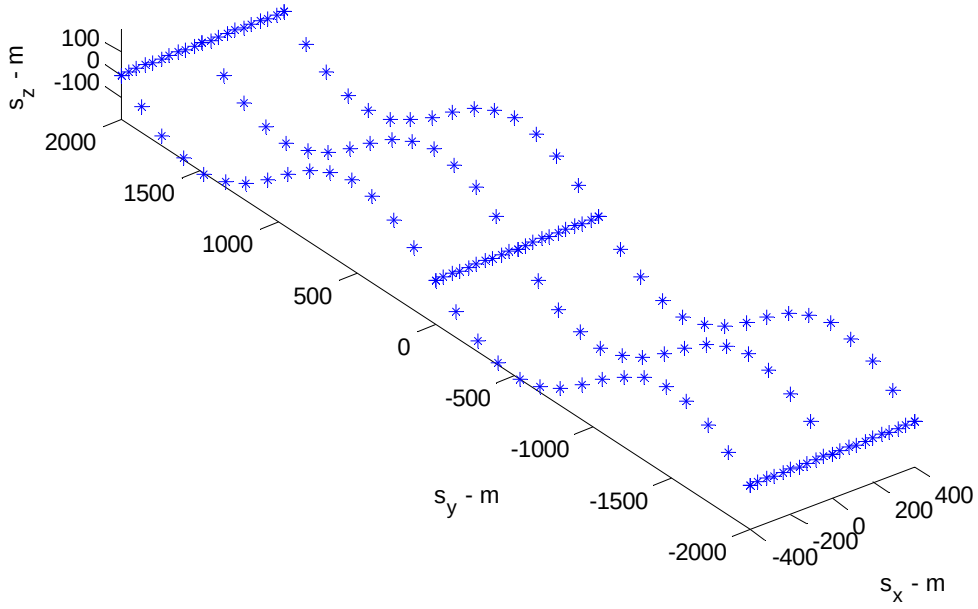

Figure 11. Example ground truth for stationary reflectors, but with height variations of 400 m peak-to-peak.

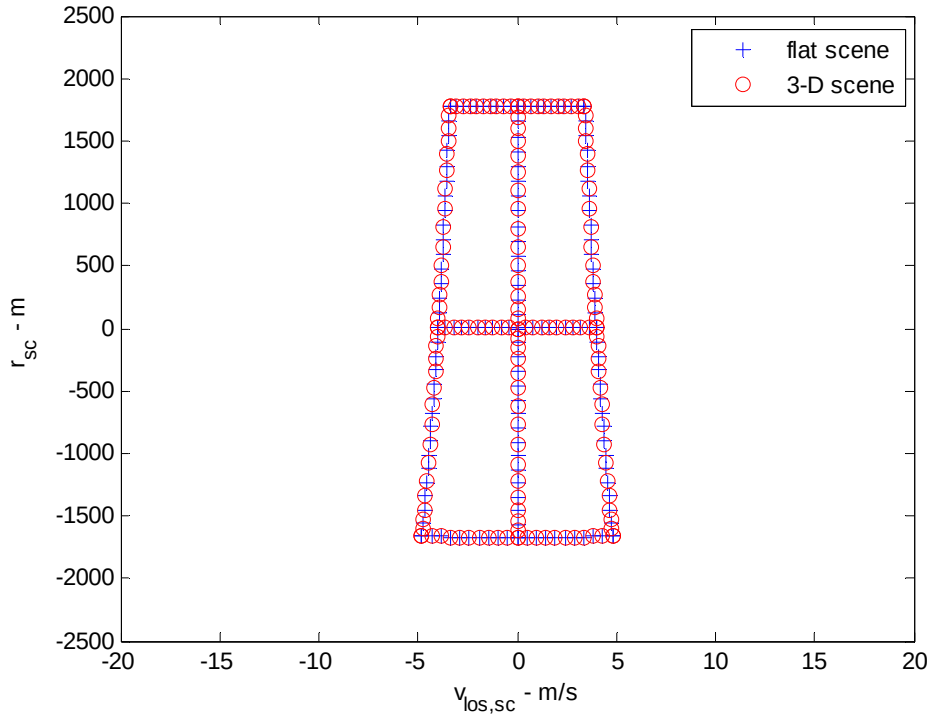

Figure 12. Range- velocity map for -90 degree squint angle.

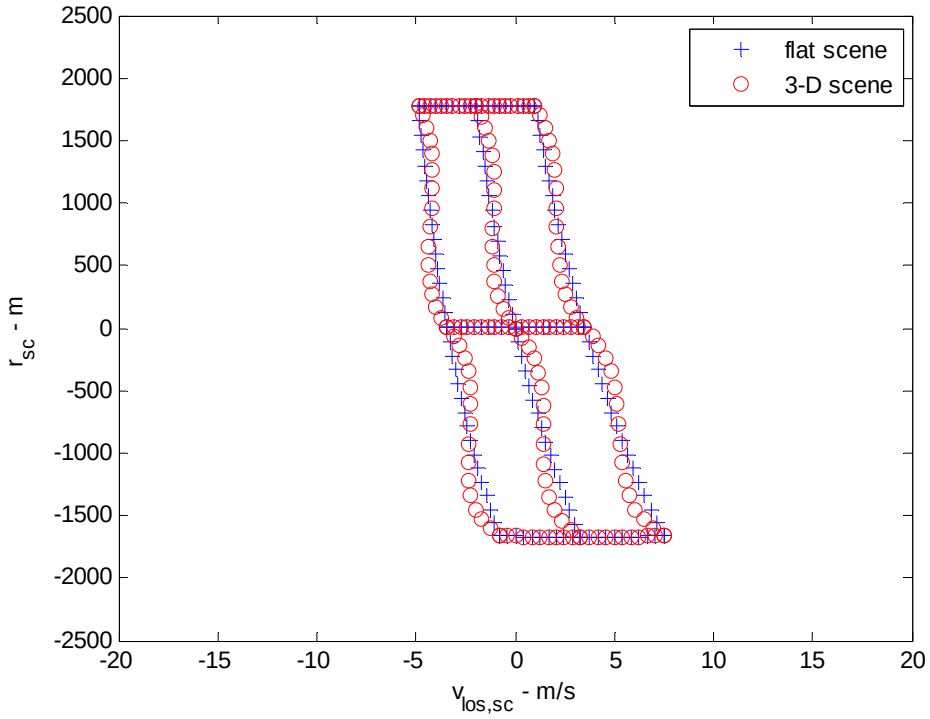

Figure 13. Range- velocity map for -60 degree squint angle.

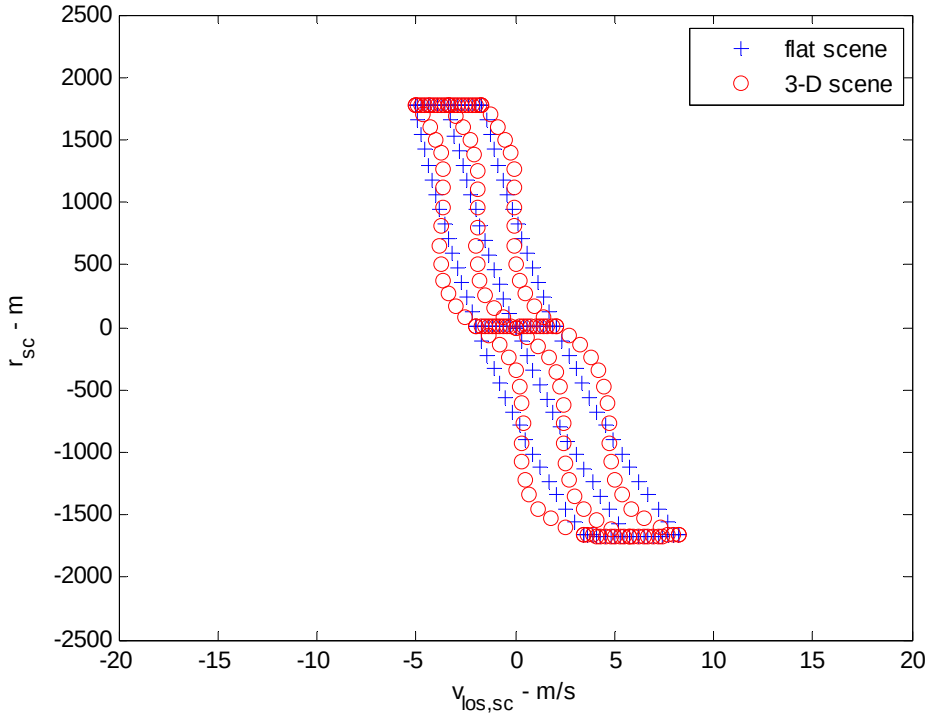

Figure 14. Range- velocity map for -30 degree squint angle.

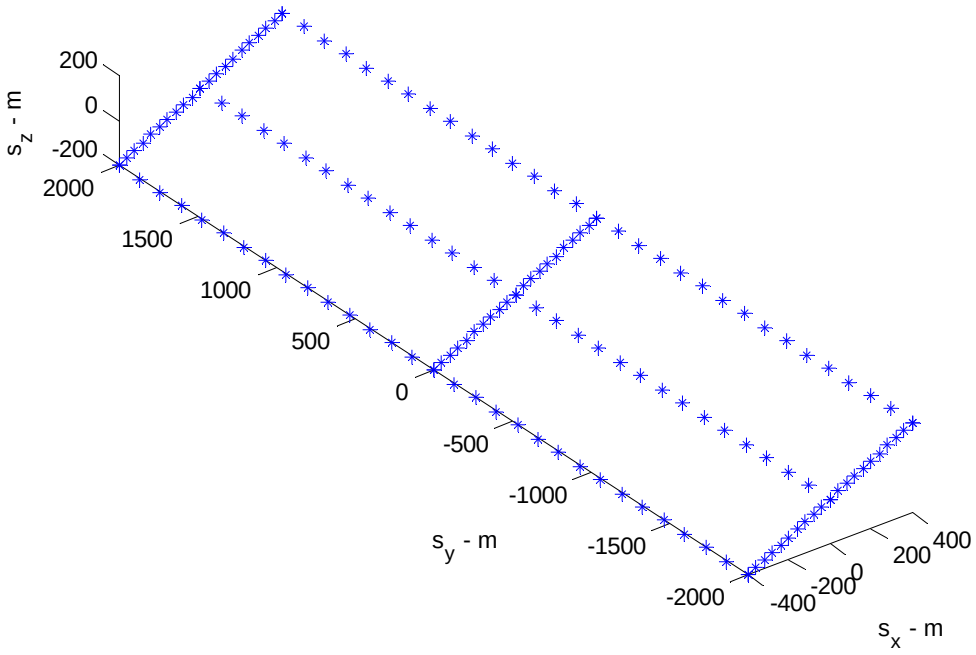

Figure 15. Example ground truth for azimuth dependent elevation variation.

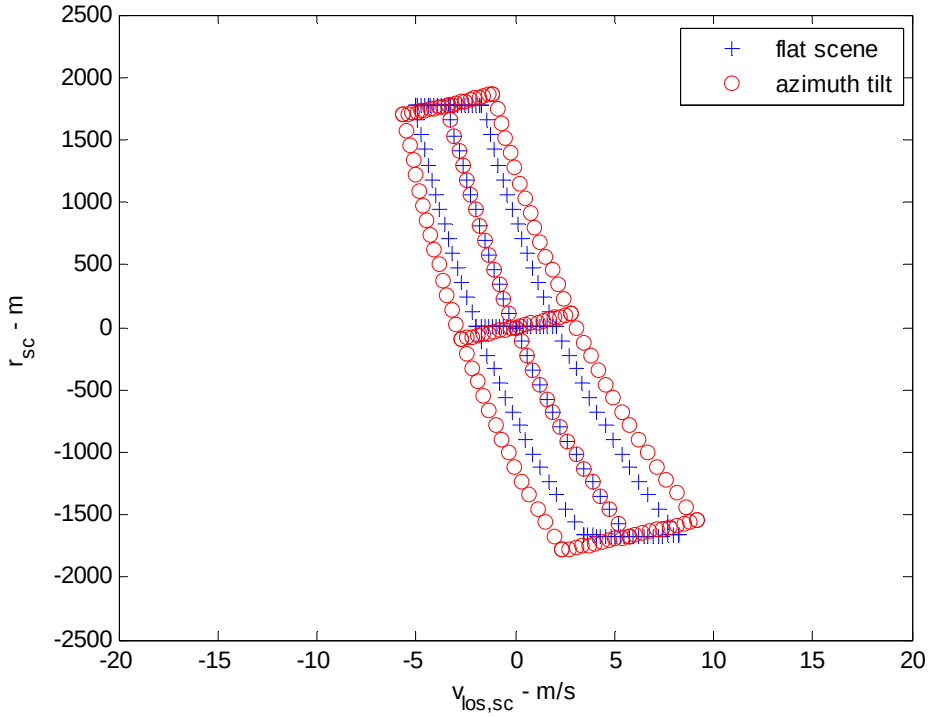

Figure 16. Range- velocity map for -30 degree squint angle.

2.3.5 Flat Terrain – Radar Vertical Velocity

In the previous sections, the radar was presumed to fly straight and level. Here we depart from this presumption, and now presume a vertical velocity component.

Example

Consider the same GMTI radar as in the previous examples, except that the radar now has a vertical velocity. Reconsider the flat target scene with stationary reflectors arranged with ground truth as in Figure 4. Figure 17 illustrates the range-Doppler map when interrogated at a –30 degree squint angle.

We observe that the scene's velocity band has shifted as a function of range, just due to the radar vertical velocity.

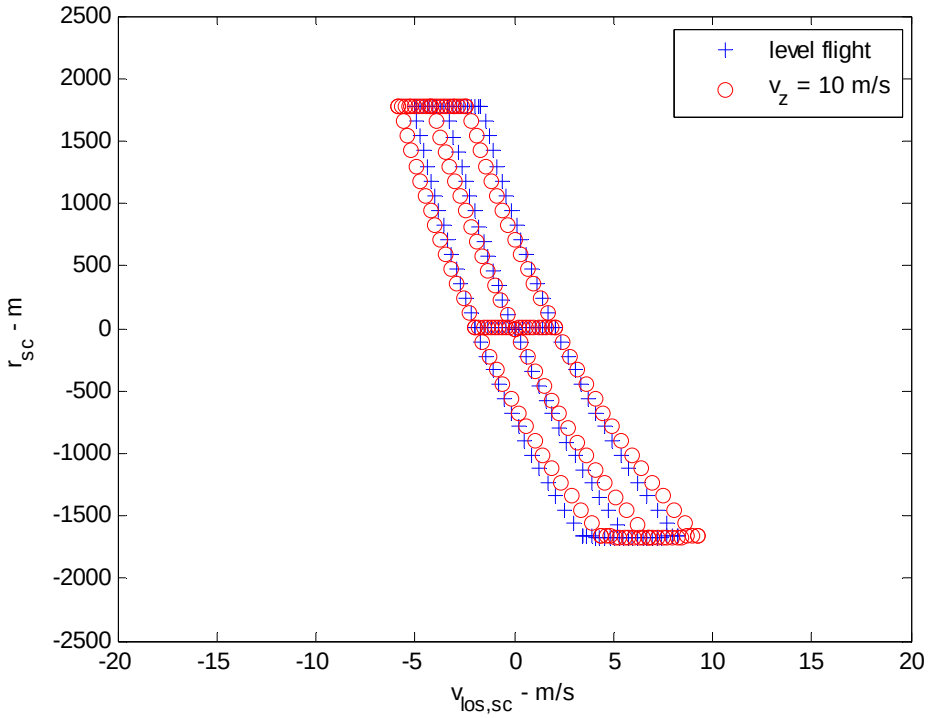

Figure 17. Range-velocity map for -30 degree squint angle.

2.4 Antenna Beam Alignment

The position and orientation of the clutter region in a range-velocity map will also depend on just what clutter is illuminated by the radar. For example, if the antenna were to exhibit an unknown pointing bias in the direction of the radar velocity vector, then the clutter band would be shifted in the range-velocity map towards more negative velocities (range-rates). Remember that the most negative range-rate is in the direction of the radar velocity vector, as this is the direction that range is decreasing the fastest.

Most radar systems have antennas that exhibit elongated antenna beam patterns, often a fan beam, where elevation beamwidth is greater (sometimes substantially so) than the azimuth beamwidth. A three-axis gimbal (or equivalent) will typically allow adequate beam rotations to a proper desired orientation and direction, most often with maximal symmetry in pan and tilt directions.

If using a two-axis gimbal, often the missing degree of freedom is one that allows for rotation around the boresight of the antenna beam, sometimes called "twist". Clearly, a rotation around the boresight for a fan-beam will cause a corresponding rotation of the footprint of the antenna beam on the ground.

This of course defines the clutter that is illuminated, and hence the basic nature of how clutter appears in a range-velocity map, quite independent of and in addition to any other factors that affect the clutter map.

We now investigate the effects of a rotation of an elliptical antenna beam.

2.4.1 The Antenna Beam Pattern Model

Consider an antenna beam where we define the angular 'edge' as an ellipse. This is illustrated in Figure 18. The equation that governs this shape is

$$\frac{\phi_h^{\,2}}{(\theta_{az}/2)^2} + \frac{\phi_v^{\,2}}{(\theta_{el}/2)^2} = 1 \tag{55}$$

where

θ_{az} = nominal azimuth beamwidth of the antenna beam,
θ_{el} = nominal elevation beamwidth of the antenna beam,
ϕ_h = horizontal offset of beam edge, and
ϕ_v = vertical offset of beam edge. (56)

With some foresight, we also identify derivative parameters

$$\tan\theta = \frac{\phi_h}{\phi_v} \tag{57}$$

and

$$\rho^2 = {\phi_h}^2 + {\phi_v}^2 . \tag{58}$$

In these terms, we can modify the ellipse equation describing the antenna beam pattern to

$$\frac{\rho^2 \sin^2\theta}{(\theta_{az}/2)^2} + \frac{\rho^2 \cos^2\theta}{(\theta_{el}/2)^2} = 1. \tag{59}$$

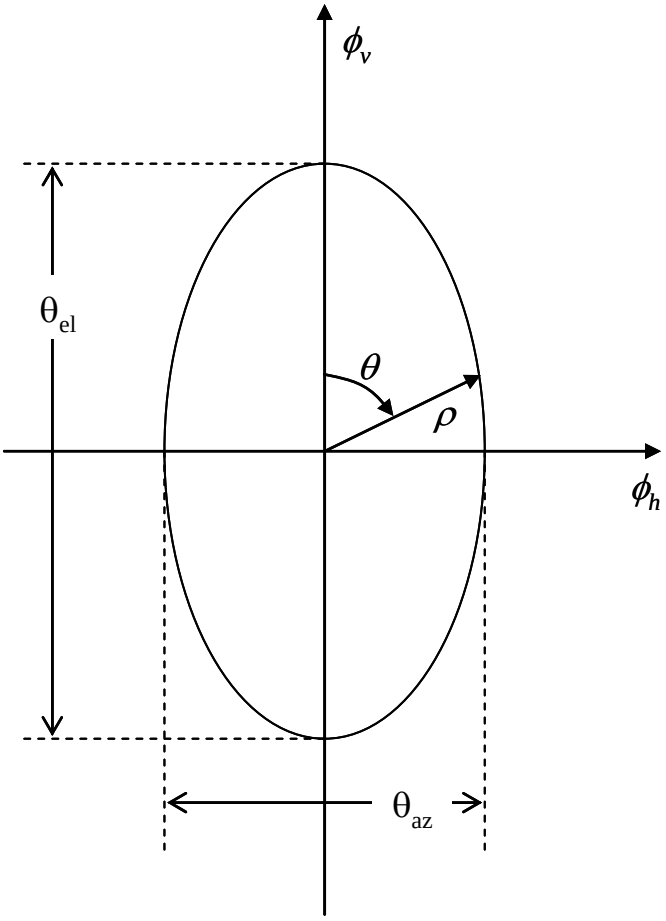

Figure 18. Model for antenna beam shape.

We may conveniently rotate the ellipse by introducing

α = antenna beam rotation about its boresight. (60)

This is illustrated in Figure 19. This causes a modification of the antenna pattern ellipse equation to

$$\frac{\rho^2 \sin^2(\theta-\alpha)}{(\theta_{az}/2)^2} + \frac{\rho^2 \cos^2(\theta-\alpha)}{(\theta_{el}/2)^2} = 1. \quad (61)$$

However, it remains true that

$$\phi_h = \rho \sin\theta$$
$$\phi_v = \rho \cos\theta. \quad (62)$$

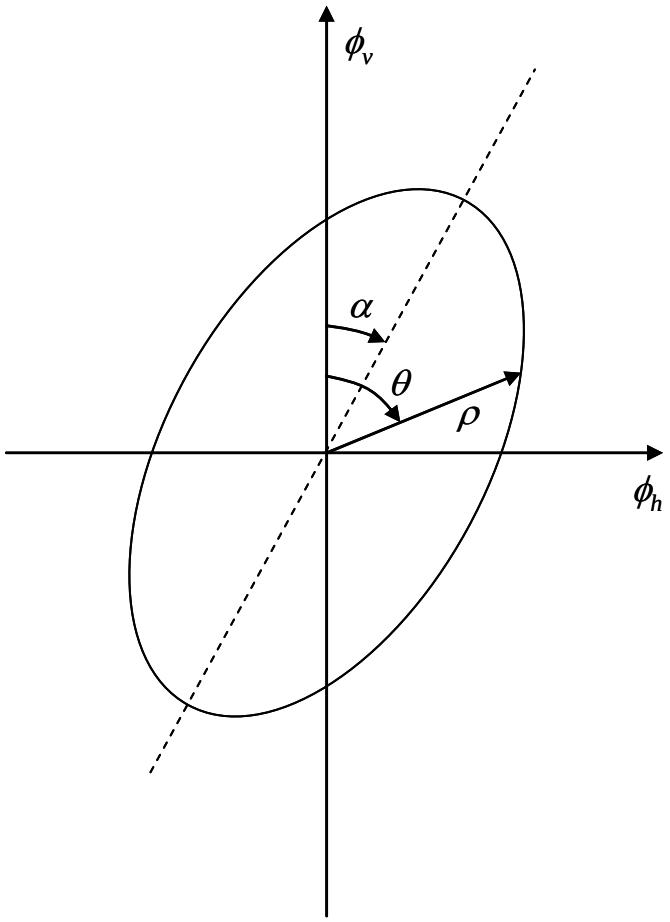

Figure 19. Model for rotated antenna beam shape.

2.4.2 The Target Scene Projection Model

We will assume that the antenna boresight is directed towards the center of the scene being interrogated. The question then becomes "How do angular offsets from the antenna boresight project onto the target plane?" We will further assume a horizontal flat target plane with no elevation offset. This is illustrated in Figure 20.

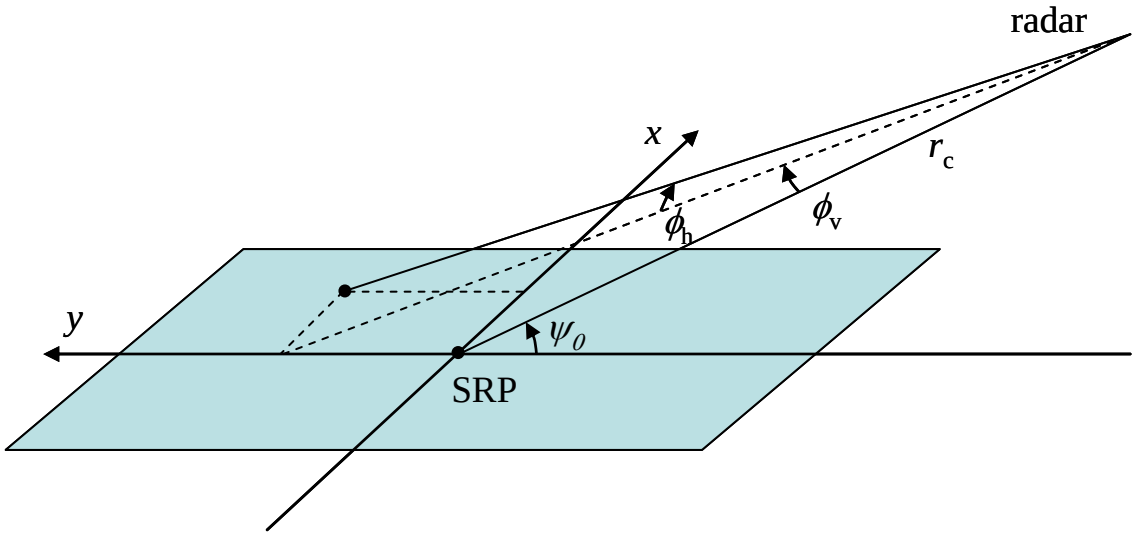

Figure 20. Target scene projection model.

It is straightforward to derive

$$x = \frac{r_c \sin\psi_0 \tan\phi_h}{\sin(\psi_0 - \phi_v)} \tag{63}$$

and

$$y = r_c \sin\psi_0 (\cot(\psi_0 - \phi_v) - \cot\psi_0). \tag{64}$$

These, with the antenna beam shape model, will allow us to plot projections of the beam shape onto the ground. We do so next.

2.4.3 Target Scene Projection Examples

What follows are several examples of projecting rotated elliptical antenna beams onto a horizontal flat ground. In all cases we will presume

$$\begin{aligned} \theta_{az} &= 3 \text{ degrees}, \\ \theta_{el} &= 7 \text{ degrees}, \\ r_c &= 10 \text{ km, and} \\ \psi_0 &= 10 \text{ degrees} \end{aligned} \tag{65}$$

We illustrate antenna rotations about its boresight of 0 degrees, 30 degrees, 60 degrees, and 90 degrees respectively in Figure 21 through Figure 24. We make several observations.

- Even for a perfectly oriented antenna, the ground projection is asymmetrical in the down-range (y) direction.
- A rotation of the antenna beam results in a rotation of the beam footprint on the ground, but the amount of rotation of the projection is not identical.
- For a vertical fan beam, the rotation for small angles is in the same direction.
- For a vertical fan beam, antenna rotation also results in a smaller range swath being illuminated.
- Even a horizontal fan beam may project longer in the down-range direction than in the cross-range (azimuth) direction. This is because of the grazing angle.

Figure 25 illustrates the relationship of rotation in the ground plane projection to the rotation of the antenna beam about its boresight for several grazing angles. Note that sensitivity for small grazing angles decreases with grazing angle. While an interesting and important characteristic, it is deceptive to monitor only this and ignore how the dimensions, particularly the aspect ratio, of the projection also changes with antenna rotation.

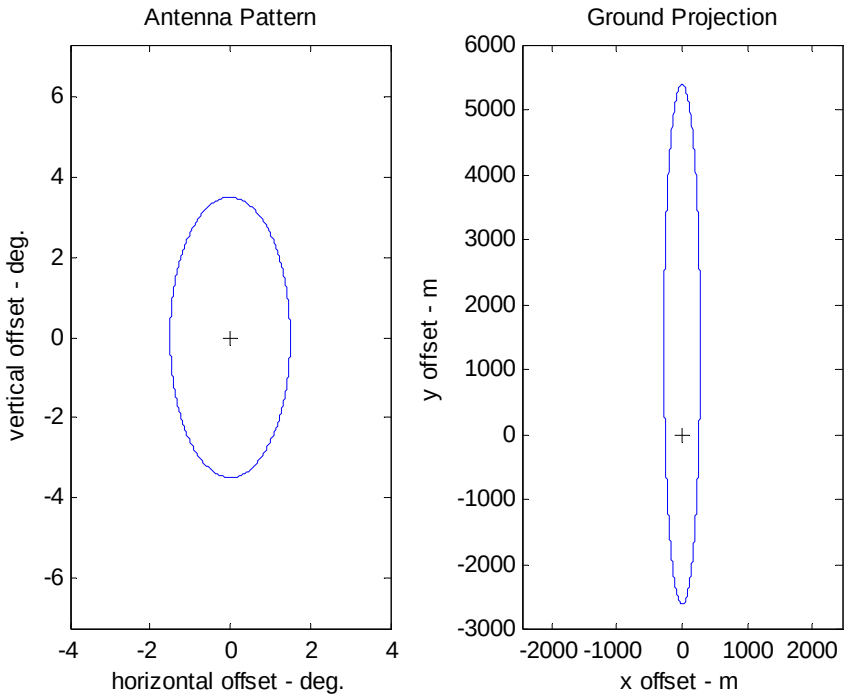

Figure 21. Antenna pattern and ground projection for 0 degrees of antenna rotation.

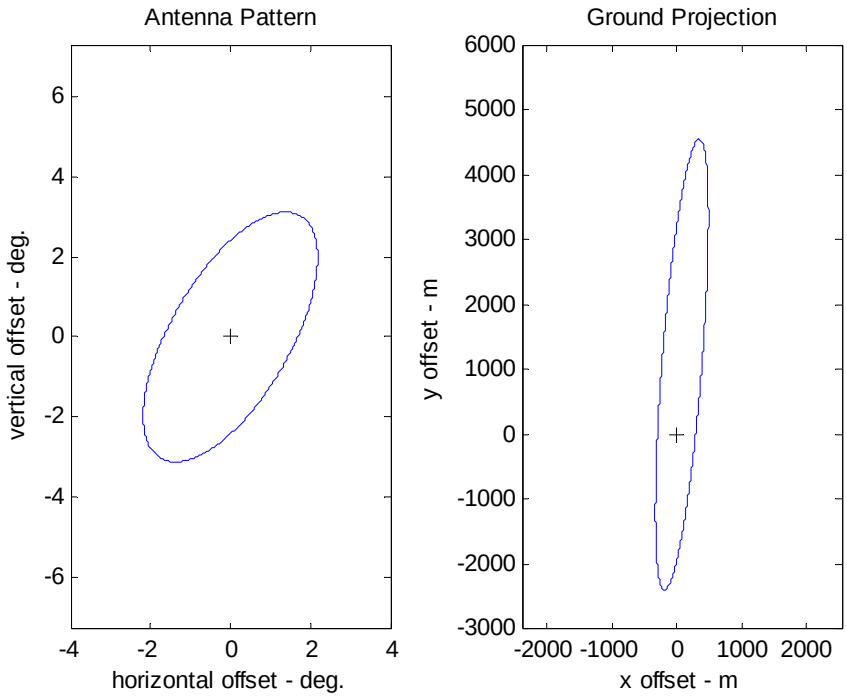

Figure 22. Antenna pattern and ground projection for 30 degrees of antenna rotation.

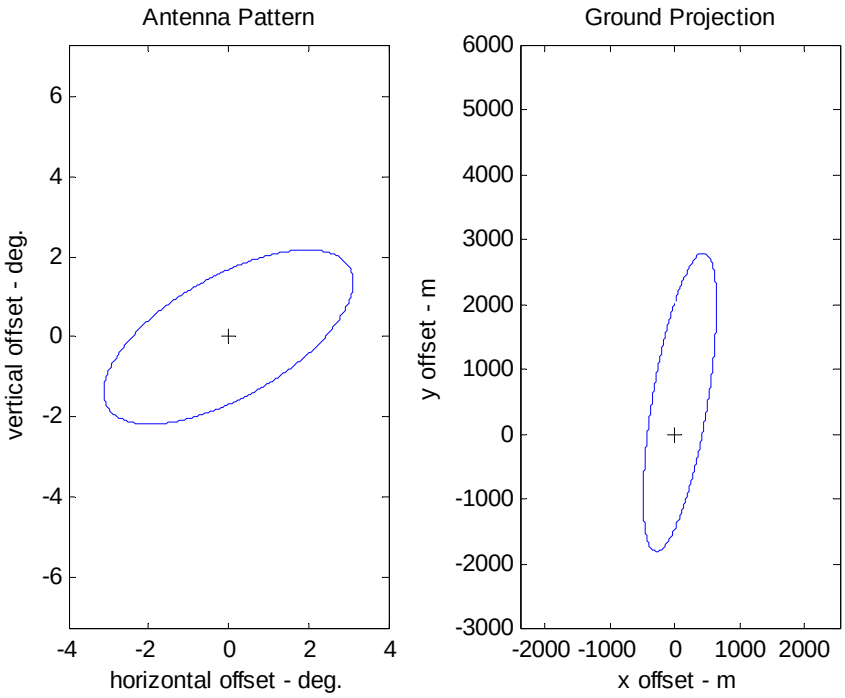

Figure 23. Antenna pattern and ground projection for 60 degrees of antenna rotation.

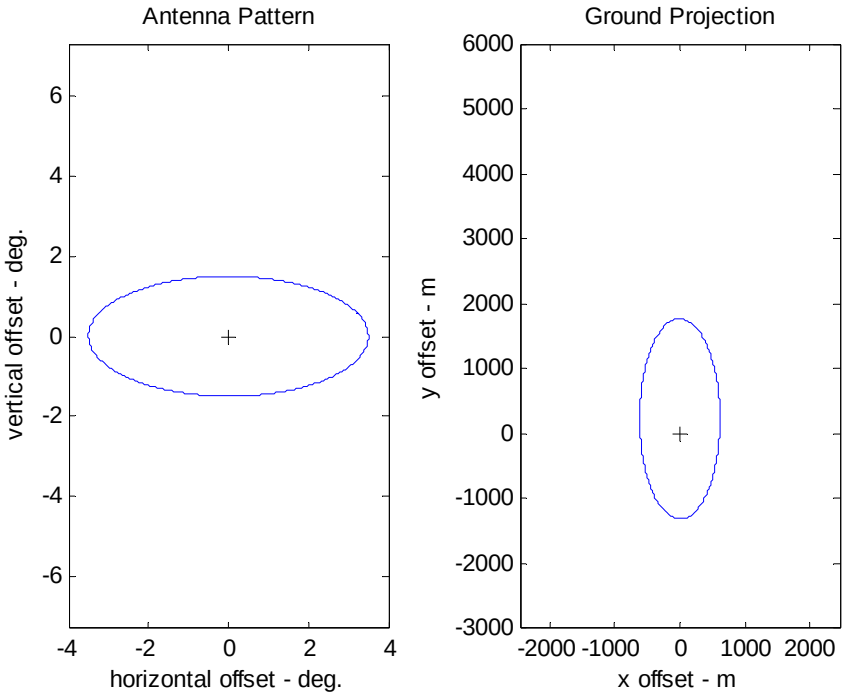

Figure 24. Antenna pattern and ground projection for 90 degrees of antenna rotation.

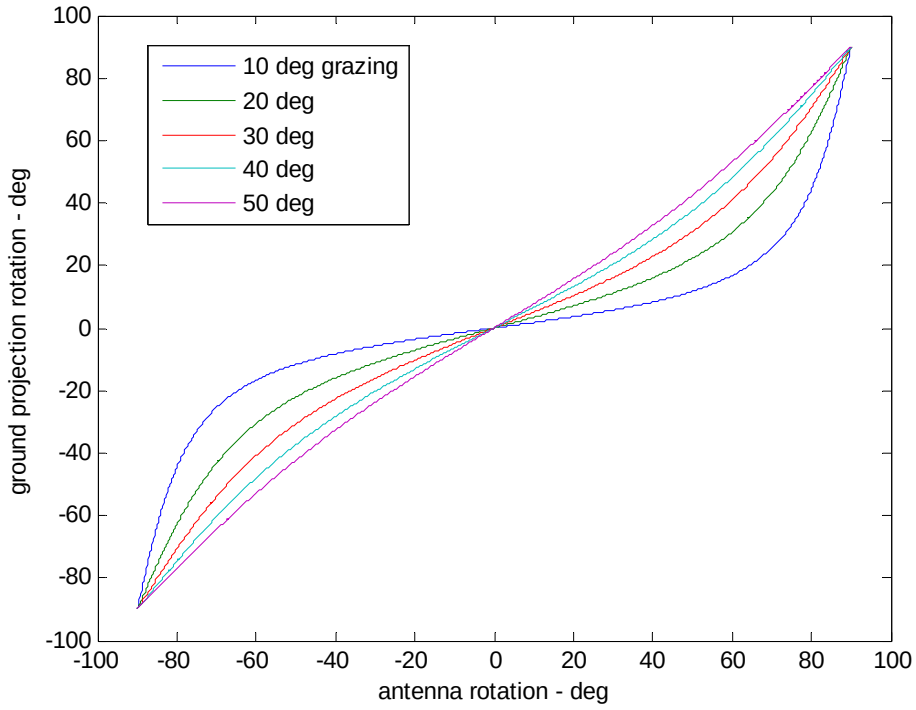

Figure 25. Ground projection rotation versus antenna rotation at various grazing angles.

2.5 Clutter Motion

Up until now, we have assumed that those target scene features that we normally assign the label as "clutter" were stationary during the course of the data collection. This might be stretching the truth somewhat. In fact, the clutter itself may, actually does, have a motion spectrum primarily due to wind. Quite simply, wind makes clutter move. This motion will broaden the Doppler spectrum of the clutter, and broaden the velocity spectrum that clutter occupies in a range-velocity map.

Skolnik[5] compiles results of other authors to indicate that windblown clutter exhibits a Gaussian distribution that is characterized by its velocity standard deviation, σ_v. The table that Skolnik presents includes

- σ_v up to 0.32 m/s for wooded hills with 40 kt wind,
- σ_v up to 1.1 m/s for sea echoes,
- σ_v up to 1.2 m/s for chaff in 25 kt wind, and
- σ_v up to 4.0 m/s for rain clouds.

Note that 1 kt ≈ 0.514 m/s.

The discussion omitted mention of mean velocity for chaff and/or rain. Things that move (e.g. chaff, rain, trash, etc.) will probably have a significant mean horizontal velocity that may be in the region of the wind mean velocity. Presumably, the mean velocity for wooded hills was near zero, since trees don't typically translate or relocate (except for very big winds). In any case, we would expect that foliage velocity is generally limited to wind velocity, and perhaps more strictly, foliage velocity is likely limited to wind velocity variations (e.g. gusts, etc.). This is likely also the case with cultural clutter items such as hanging objects. Windmills, fans, and turbines are a different story.

Nathanson[6] shows data that suggests that the –3 dB velocity bandwidth of sea clutter is related to Hydrographic Sea State, *S*, by the approximation

$$B_v \approx \frac{S}{2} \text{ m/s.} \tag{66}$$

2.6 Summary Discussion

The location, width, and shape of the clutter in a range-velocity map are influenced by any of a number of scene and radar flight parameters, including

Radar horizontal velocity
Radar squint angle
Radar vertical velocity
Radar antenna beam footprint

Target scene elevation offset
Target scene elevation variations in range
Target scene elevation variations in azimuth
Target scene composition and wind effects

An accurate prediction of how the clutter will map into range-velocity space will depend on all of these.

2.7 Clutter Mitigation

In exo-clutter GMTI, clutter is a source of false alarms. To mitigate the effects of clutter on false alarms, the GMTI needs to ignore detections in range-velocity regions that correspond to clutter. For this to occur, the radar needs to know (or calculate) where clutter topography maps into range-velocity space.

Three general classes of techniques may be employed to mitigate topography effects.

1. The radar is given topography information to estimate the location of clutter in range-velocity space. This may be in the form of Digital Terrain Elevation Data (DTED) input from a library. The radar also needs antenna attitude information.

2. The radar makes its own topography measurements, perhaps in a manner similar to Interferometric Synthetic Aperture Radar (InSAR or IFSAR). This requires a second antenna phase center in elevation. The radar still also needs antenna attitude information.

3. The radar estimates whether a pixel in the range-velocity map belongs to clutter or not based on the range-velocity map itself. This is a data-driven adaptive technique. Basically, the radar tries to ‘detect’ the clutter and identify it as such.

In all cases, accurate and precise radar motion information is required.

Of course, combinations and variations of these basic ideas may also be useful.

“Get your facts first, then you can distort them as you please.”

-- Mark Twain

3 Conclusions

The following points are worth repeating.

- In exo-clutter GMTI radars, the ground clutter generates false alarms. This is undesirable.

- GMTI radars need to ignore detections in regions of clutter. To do this, the radar needs to know how clutter maps into range-velocity space for the radar.

- The nature of how clutter maps into range-velocity space for GMTI depends on a number of factors, including generally radar motion and viewing geometry, and the topography of the target scene.

- The radar can determine the clutter characteristics in its range-velocity space by several different techniques. These include using radar motion/attitude information with target scene topography, or perhaps by trying to 'detect' the clutter based on the data itself. Additionally, the radar may measure the target scene topography using other techniques such as IFSAR. Combinations of these may also be used.

Figure 26. Christian Andreas Doppler (29 November 1803 – 17 March 1853) was an Austrian mathematician and physicist. The Doppler effect is named after him. The Doppler effect is an apparent change in frequency and wavelength due to relative motion between a wave's source and an observer.

Appendix A – The Phase History Model

In this appendix we develop a model for the radar's phase history data as collected by a GMTI radar using stretch processing.

We will also presume that the GMTI radar dwells on a reference location for the duration of its Coherent Processing Interval (CPI). We name this reference location as the Scene Reference Point (SRP) and designate it as the origin of the coordinate frame used for data collection and processing.

We apologize up front for this being an exercise in keeping track of all the various subscripts.

The Radar Signals

In general, the radar will collect data over a CPI using N pulses. We allow the pulse index n to vary as

$$\frac{-N}{2} \le n < \frac{N}{2}. \tag{A1}$$

At some range from the SRP the radar emits a pulse towards the SRP which we model as

$$X_T(t,n) = \text{rect}\left(\frac{(t-t_n)}{T}\right)\exp\left\{ j\left(\phi_{T,n} + \omega_{T,n}(t-t_n) + \frac{\gamma_{T,n}}{2}(t-t_n)^2 \right)\right\} \tag{A2}$$

where

t_n = the reference time for pulse n ,
T = the transmitted pulse width,
$\phi_{T,n}$ = the reference phase for transmitted pulse n,
$\omega_{T,n}$ = the reference radian frequency for transmitted pulse n,
$\gamma_{T,n}$ = the radian chirp rate for transmitted pulse n. (A3)

We define the pulse envelope function

$$\text{rect}(x) = \begin{cases} 1 & |x| \le 1/2 \\ 0 & else \end{cases}. \tag{A4}$$

The received echo signal is a delayed and attenuated version of the transmitted signal.

$$X_R(t,n) = A_r \,\mathrm{rect}\left(\frac{(t - t_n - t_s)}{T}\right)\exp\left\{ j\left(\begin{array}{l} \phi_{T,n} \\ +\omega_{T,n}(t - t_n - t_s) \\ +\frac{\gamma_{T,n}}{2}(t - t_n - t_s)^2 \end{array} \right)\right\} \tag{A5}$$

where

t_s = the echo delay time for pulse *n*,
A_R = the modified signal amplitude of the received echo. (A6)

Recall that we are generally presuming a relative motion between radar and target, consequently any echo delay time will itself be time-dependent. While not explicitly shown, t_s is itself a function of time.

We will presume that our GMTI uses stretch processing, whereby the received echoes are 'dechirped' with a Local Oscillator signal modeled as

$$X_{LO}(t,n) = \mathrm{rect}\left(\frac{(t - t_n - t_m)}{T_L}\right)\exp\left\{ j\left(\phi_{L,n} + \omega_{L,n}(t - t_n - t_m) + \frac{\gamma_{L,n}}{2}(t - t_n - t_m)^2 \right)\right\} \tag{A7}$$

where

t_m = the Local Oscillator reference offset time,
T_L = the Local Oscillator pulse width,
$\phi_{L,n}$ = the reference phase for Local Oscillator pulse *n*,
$\omega_{L,n}$ = the reference radian frequency for Local Oscillator pulse *n*,
$\gamma_{L,n}$ = the radian chirp rate for Local Oscillator pulse *n*. (A8)

Application of the Local Oscillator signal to the received echo yields a video difference signal of the form

$$X_V(t,n) = A_r \,\mathrm{rect}\left(\frac{\left(t - t_n - t_{s,}\right)}{T}\right)\mathrm{rect}\left(\frac{\left(t - t_n - t_m\right)}{T_L}\right)$$
$$\times \exp\left\{ j\left(\begin{array}{l} \phi_{T,n} - \phi_{L,n} \\ +\omega_{T,n}\left(t - t_n - t_s\right) - \omega_{L,n}\left(t - t_n - t_m\right) \\ +\frac{\gamma_{T,n}}{2}\left(t - t_n - t_s\right)^2 - \frac{\gamma_{L,n}}{2}\left(t - t_n - t_m\right)^2 \end{array} \right) \right\}. \qquad \text{(A9)}$$

This signal is sampled by the Analog to Digital Converter (ADC) at times

$$t = t_n + t_m + T_s i \qquad \text{(A10)}$$

where

T_s = the ADC sample spacing
i = the ADC sampling index within a single pulse. (A11)

We allow for a multitude of samples totaling I, with index i such that

$$\frac{-I}{2} \le i < \frac{I}{2}. \qquad \text{(A12)}$$

At this point we observe that ADC sample times span an interval of $T_s I$. As previously noted, during this time both target and aircraft are moving. Consequently the target delay is in fact changing during the time we are sampling, as well as on a pulse to pulse basis. We now explicitly show t_s as a function of indices i and n, and model this as

$$t_s = t_{s,n,i} = t_{s,n,0} + \left(\frac{d}{d\left(T_s i\right)} t_{s,n,i}\right) T_s i \,. \qquad \text{(A13)}$$

The resulting video signal is then described by

$$X_V(i,n) = A_r \exp\left\{ j \left(\begin{array}{l} \phi_{T,n} - \phi_{L,n} \\ + \omega_{T,n}\left(T_s i + t_m - t_{s,n,0} - \left(\frac{d}{d(T_s i)} t_{s,n,i} \right) T_s i \right) - \omega_{L,n}(T_s i) \\ + \frac{\gamma_{T,n}}{2}\left(T_s i + t_m - t_{s,n,0} - \left(\frac{d}{d(T_s i)} t_{s,n,i} \right) T_s i \right)^2 - \frac{\gamma_{L,n}}{2}(T_s i)^2 \end{array} \right) \right\}. \quad \text{(A14)}$$

We manipulate this to

$$X_V(i,n) = A_r \exp\left\{ j \left(\begin{array}{l} \phi_{T,n} - \phi_{L,n} \\ + \omega_{T,n}\left(\left(1 - \frac{d}{d(T_s i)} t_{s,n,i} \right) T_s i + t_m - t_{s,n,0} \right) - \omega_{L,n}(T_s i) \\ + \frac{\gamma_{T,n}}{2}\left(\left(1 - \frac{d}{d(T_s i)} t_{s,n,i} \right) T_s i + t_m - t_{s,n,0} \right)^2 - \frac{\gamma_{L,n}}{2}(T_s i)^2 \end{array} \right) \right\}. \quad \text{(A15)}$$

As a part of real-time motion compensation, we equate

$$\begin{aligned} &\phi_{L,n} = \phi_{T,n}, \\ &\omega_{L,n} = \omega_{T,n}\left(1 - \frac{d}{d(T_s i)} t_{s,n,i} \right), \text{ and} \\ &\gamma_{L,n} = \gamma_{T,n}\left(1 - \frac{d}{d(T_s i)} t_{s,n,i} \right)^2. \end{aligned} \quad \text{(A16)}$$

This simplifies the video signal model to

$$X_V(i,n) = A_r \exp\left\{ j \left(\begin{array}{l} \left[\omega_{T,n} + \gamma_{T,n}\left(1 - \frac{d}{d(T_s i)} t_{s,n,i} \right) T_s i \right] (t_m - t_{s,n,0}) \\ + \frac{\gamma_{T,n}}{2}(t_m - t_{s0,n})^2 \end{array} \right) \right\}. \quad \text{(A17)}$$

In SAR we often modulate frequency and chirp rate to facilitate mitigation of migration terms, which is necessary for fine resolution imaging. For GMTI, CPIs are short enough

and range resolution is typically coarse enough that migration is not a significant problem.

In a manner similar to target echo delay time, the echo delay time to the SRP is also time dependent and can be expressed as

$$t_c = t_{c,n,i} = t_{c,n,0} + \left(\frac{d}{d(T_s i)} t_{c,n,i} \right) T_s i \,. \tag{A18}$$

We note in the first line of the phase term the overt dependence on the time-dependent echo delay time, namely what we will identify later as a dependence on the line-of-sight velocity. We might to advantage compensate this term somewhat by modulating

$$\gamma_{T,n} = \frac{\gamma_{T,0}}{\left(1 - \frac{d}{d(T_s i)} t_{c,n,i} \right)} \tag{A19}$$

for some constant $\gamma_{T,0}$. This would yield a video signal of the form

$$X_V(i,n) = A_r \exp\left\{ j\left(\left[\omega_{T,n} + \gamma_{T,0} \left(\frac{1 - \frac{d}{d(T_s i)} t_{s,n,i}}{1 - \frac{d}{d(T_s i)} t_{c,n,i}} \right) T_s i \right] \left(t_m - t_{s,n,0} \right) + \frac{\gamma_{T,n}}{2} \left(t_m - t_{s,n,0} \right)^2 \right) \right\} \tag{A20}$$

or approximately

$$X_V(i,n) = A_r \exp\left\{ j\left(\left[\omega_{T,n} + \gamma_{T,0} \left(1 - \left(\frac{d}{d(T_s i)} t_{s,n,i} - \frac{d}{d(T_s i)} t_{c,n,i} \right) \right) T_s i \right] \left(t_m - t_{s,n,0} \right) + \frac{\gamma_{T,n}}{2} \left(t_m - t_{s,n,0} \right)^2 \right) \right\} \tag{A21}$$

with a substantially reduced influence by the radar velocity. Nevertheless, we will presume constant reference frequency and allow for a chirp rate modulated in this fashion or not by defining a parameter ζ_n such that

$$\zeta_n = \begin{cases} \left(\dfrac{d}{d(T_s i)} t_{s,n,i} - \dfrac{d}{d(T_s i)} t_{c,n,i} \right) & \text{if we modulate } \gamma_{T,n} \\ \dfrac{d}{d(T_s i)} t_{s,n,i} & \text{if we don't} \end{cases} . \tag{A22}$$

Sandia-designed GMTI modes designed to date do in fact modulate the chirp rate in this fashion. The model then becomes

$$X_V(i,n) = A_r \exp\left\{ j \begin{pmatrix} -\left[\omega_{T,0} + \gamma_{T,0}(1-\zeta_n) T_s i\right]\left(t_{s,n,0} - t_m\right) \\ + \dfrac{\gamma_{T,0}}{2}\left(t_{s,n,0} - t_m\right)^2 \end{pmatrix} \right\} . \tag{A23}$$

The term in the second line of the phase of this expression is the Residual Video Phase Error (RVPE) term. It can frequently be mitigated with processing, but is often ignored for coarse resolution processing, too. We will carry it along for now.

Radar Geometry and Motion

In general, the target location and the radar location will both vary with time, we define these time-dependent locations as

$\mathbf{s}(t)$ = the vector describing the location of the target, and
$\mathbf{r}_c(t)$ = the vector describing the location of the radar. (A24)

These are illustrated in Figure 27.

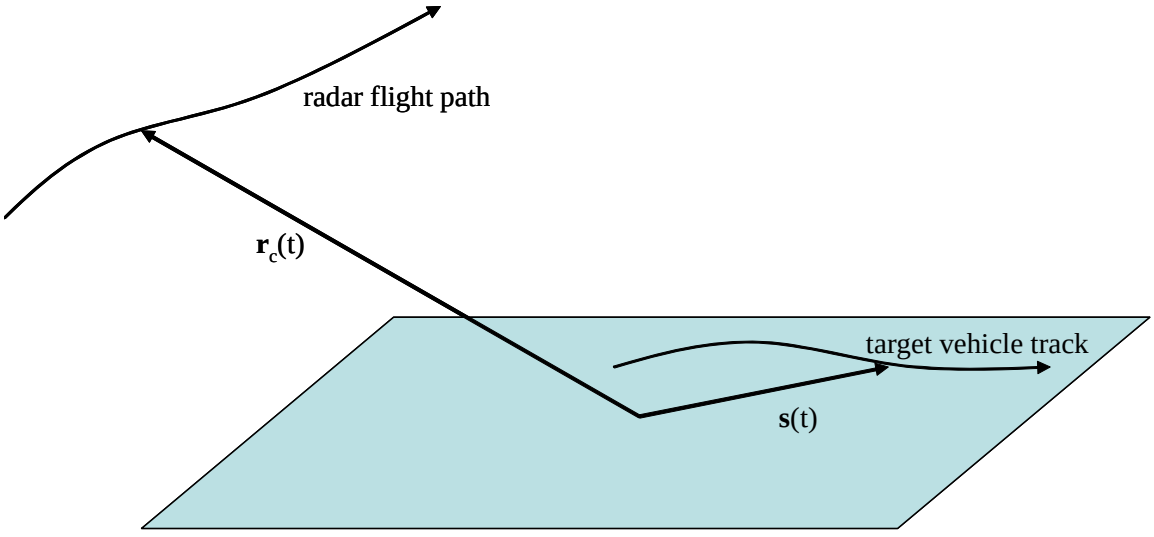

Figure 27. Geometry definitions.

Time-varying quantities will vary with both indices *n* and *i*. We define time-varying vector quantities that depend on these indices as follows.

$\mathbf{s}_{n,i}$ = the vector describing the location of the target for pulse *n* and sample *i*,
$\mathbf{r}_{c,n,i}$ = the vector describing the location of the radar for pulse *n* and sample *i*.

(A25)

We identify velocities as the respective time derivatives of location, namely

$$\mathbf{v}_t = \frac{d}{dt}\mathbf{s}(t) \text{ = target velocity vector, and}$$
$$\mathbf{v}_c = \frac{d}{dt}\mathbf{r}_c(t) \text{ = radar velocity vector.} \quad \text{(A26)}$$

We will assume these velocities to be constant during a CPI.

Furthermore, we identify

$$\mathbf{r}_s(t) = \mathbf{r}_c(t) - \mathbf{s}(t) \text{ = vector of radar location relative to target,}$$
$$\mathbf{v}_s = \mathbf{v}_c - \mathbf{v}_t \text{ = radar velocity relative to target.} \quad \text{(A27)}$$

Consequently, we can equate

$$\mathbf{r}_s(t) = \mathbf{r}_s(t_n + t_m + T_s i) + (t - t_n - t_m - T_s i)\mathbf{v}_s,$$
$$\mathbf{r}_c(t) = \mathbf{r}_c(t_n + t_m + T_s i) + (t - t_n - t_m - T_s i)\mathbf{v}_c, \text{ and}$$
$$\mathbf{s}_n(t) = \mathbf{s}_n(t_n + t_m + T_s i) + (t - t_n - t_m - T_s i)\mathbf{v}_t. \quad \text{(A28)}$$

We define range as a scalar equal to the magnitude of location vectors. That is

$$r_{s,n,i} = |\mathbf{r}_s(t_n + t_m + T_s i)| \text{ = range to the target, and}$$
$$r_{c,n,i} = |\mathbf{r}_c(t_n + t_m + T_s i)| \text{ = range to scene center.} \quad \text{(A29)}$$

The following scalar line-of-sight velocities are also useful

$$v_{los,s}(t) = \frac{d}{dt}|\mathbf{r}_s(t)| = \frac{\mathbf{r}_s(t)}{|\mathbf{r}_s(t)|} \bullet \mathbf{v}_s,$$
$$v_{los,c}(t) = \frac{d}{dt}|\mathbf{r}_c(t)| = \frac{\mathbf{r}_c(t)}{|\mathbf{r}_c(t)|} \bullet \mathbf{v}_c, \text{ and}$$
$$v_{los,t}(t) = \frac{\mathbf{r}_s(t)}{|\mathbf{r}_s(t)|} \bullet \mathbf{v}_t. \quad \text{(A30)}$$

Over short CPIs and for expected target vehicle motions, we will presume these to be adequately modeled as constants. In general, $v_{los,c}(t)$ is known, but $v_{los,s}(t)$ and $v_{los,t}(t)$ are not.

We note that

$$v_{los,s}(t) = \frac{\mathbf{r}_s(t)}{|\mathbf{r}_s(t)|} \bullet (\mathbf{v}_c - \mathbf{v}_t). \tag{A31}$$

This relationship can also be rewritten and expressed as

$$v_{los,s}(t) = \left(v_{los,c}(t) + \left(\frac{\mathbf{r}_s(t)}{|\mathbf{r}_s(t)|} - \frac{\mathbf{r}_c(t)}{|\mathbf{r}_c(t)|} \right) \bullet \mathbf{v}_c - \frac{\mathbf{r}_s(t)}{|\mathbf{r}_s(t)|} \bullet \mathbf{v}_t \right) \tag{A32}$$

or

$$v_{los,s}(t) - v_{los,c}(t) = \left(\frac{\mathbf{r}_s(t)}{|\mathbf{r}_s(t)|} - \frac{\mathbf{r}_c(t)}{|\mathbf{r}_c(t)|} \right) \bullet \mathbf{v}_c - v_{los,t}(t). \tag{A33}$$

At particular sample times,

$$\begin{aligned} v_{los,s,n,i} &= \frac{\mathbf{r}_s(t_n + t_m + T_s i)}{|\mathbf{r}_s(t_n + t_m + T_s i)|} \bullet \mathbf{v}_s, \\ v_{los,c,n,i} &= \frac{\mathbf{r}_c(t_n + t_m + T_s i)}{|\mathbf{r}_c(t_n + t_m + T_s i)|} \bullet \mathbf{v}_c, \text{ and} \\ v_{los,t,n,i} &= \frac{\mathbf{r}_s(t_n + t_m + T_s i)}{|\mathbf{r}_s(t_n + t_m + T_s i)|} \bullet \mathbf{v}_t. \end{aligned} \tag{A34}$$

<u>Radar Echo Delays</u>

Echo time delays are related to range by the velocity of propagation. Specifically,

$$\begin{aligned} t_s &= \frac{2}{c} |\mathbf{r}_s(t)|, \text{ and} \\ t_c &= \frac{2}{c} |\mathbf{r}_c(t)|, \end{aligned} \tag{A35}$$

where

c = the velocity of propagation. (A36)

In terms of sample times,

$$t_{s,n,i} = \frac{2}{c} r_{s,n,i} \text{ , and}$$
$$t_{c,n,i} = \frac{2}{c} r_{c,n,i} \text{ .} \tag{A37}$$

We also recognize that

$$\frac{d}{d(T_s i)} t_{s,n,i} = \frac{2}{c} \frac{d}{d(T_s i)} r_{s,n,i} = \frac{2}{c} v_{los,s,n,i} \text{ , and}$$
$$\frac{d}{d(T_s i)} t_{c,n,i} = \frac{2}{c} \frac{d}{d(T_s i)} r_{c,n,i} = \frac{2}{c} v_{los,c,n,i} \text{ .} \tag{A38}$$

It is adequate to model

$$v_{los,s,n,i} \approx v_{los,s,n,0} \text{ , and}$$
$$v_{los,c,n,i} \approx v_{los,c,n,0} \text{ .} \tag{A39}$$

Our model for the video phase history data remains

$$X_V(i,n) = A_r \exp\left\{ j \left(\begin{array}{l} -\left[\omega_{T,0} + \gamma_{T,0}(1-\zeta_n) T_s i\right]\left(t_{s,n,0} - t_m\right) \\ + \frac{\gamma_{T,0}}{2}\left(t_{s,n,0} - t_m\right)^2 \end{array} \right) \right\} \tag{A40}$$

where we now identify

$$\zeta_n = \begin{cases} \frac{2}{c}\left(v_{los,s,n,0} - v_{los,c,n,0}\right) & \text{if we modulate} \gamma_{T,n} \\ \frac{2}{c} v_{los,s,n,0} & \text{if we don't} \end{cases} . \tag{A41}$$

<u>Pulse to Pulse Variations</u>

We now turn our attention to the target delay characteristics and how they change from pulse to pulse. The target delay term $t_{s0,n}$ is modeled to be static during a pulse, but varies from one pulse to the next. By assuming a constant Pulse Repetition Frequency (PRF) we can model this as

$$t_{s,n,0} = \frac{2}{c} r_{s,n,0} \approx \frac{2}{c}\left(r_{s,0,0} + v_{los,s,0,0} T_p n\right) \tag{A42}$$

where

$r_{s,0,0}$ = nominal target range at center of CPI, and
T_p = the pulse period = 1/PRF. (A43)

We furthermore identify the SRP delay as

$$t_{c,n,0} = \frac{2}{c} r_{c,n,0} \approx \frac{2}{c}\left(r_{c,0,0} + v_{los,c,0,0} T_p n\right) \tag{A44}$$

where

$r_{c,0,0}$ = nominal range to the SRP at center of CPI. (A45)

We choose to operate the radar so that the Local Oscillator reference time tracks the delay from the scene center, namely

$$t_m = t_{c,n,0}\,. \tag{A46}$$

We consequently calculate the relative target delay as

$$\left(t_{s,n,0} - t_m\right) = \frac{2}{c}\left(r_{s,n,0} - r_{c,n,0}\right) = \frac{2}{c}\left(r_{s,0,0} - r_{c,0,0}\right) + \frac{2}{c}\left(v_{los,s,0,0} - v_{los,c,0,0}\right) T_p n\,. \tag{A47}$$

Combining this into the video phase history model yields

$$X_V(i,n) = A_r \exp\left\{ j\left(\begin{array}{l} -\left[\omega_{T,0} + \gamma_{T,0}\left(1-\zeta_n\right) T_s i\right]\left(\begin{array}{l} \frac{2}{c}\left(r_{s,0,0} - r_{c,0,0}\right) \\ + \frac{2}{c}\left(v_{los,s,0,0} - v_{los,c,0,0}\right) T_p n \end{array} \right) \\ + \frac{\gamma_{T,0}}{2}\left(\frac{2}{c}\left(r_{s,0,0} - r_{c,0,0}\right) + \frac{2}{c}\left(v_{los,s,0,0} - v_{los,c,0,0}\right) T_p n \right)^2 \end{array} \right) \right\}. \tag{A48}$$

We parse the various phase terms to yield

$$X_V(i,n) = A_r \exp\left\{ j \left(\begin{array}{l} -\frac{2}{c}\omega_{T,0}\left(r_{s,0,0} - r_{c,0,0}\right) \\ -\frac{2}{c}\gamma_{T,0}\left(1-\zeta_n\right)\left(r_{s,0,0} - r_{c,0,0}\right)T_s i \\ -\frac{2}{c}\omega_{T,0}\left(v_{los,s,0,0} - v_{los,c,0,0}\right)T_p n \\ -\frac{2}{c}\gamma_{T,0}\left(1-\zeta_n\right)\left(v_{los,s,0,0} - v_{los,c,0,0}\right)T_p n T_s i \\ +\frac{\gamma_{T,0}}{2}\left(\frac{2}{c}\left(r_{s,0,0} - r_{c,0,0}\right) + \frac{2}{c}\left(v_{los,s,0,0} - v_{los,c,0,0}\right)T_p n\right)^2 \end{array} \right) \right\} \quad \text{(A49)}$$

or

$$X_V(i,n) = A_r \exp\left\{ j \left(\begin{array}{l} -\frac{2\omega_{T,0}}{c}\left(r_{s,0,0} - r_{c,0,0}\right) + \frac{2\gamma_{T,0}}{c^2}\left(r_{s,0,0} - r_{c,0,0}\right)^2 \\ -\frac{2\gamma_{T,0}}{c}\left(1-\zeta_n\right)\left(r_{s,0,0} - r_{c,0,0}\right)T_s i \\ -\frac{2\omega_{T,0}}{c}\left(v_{los,s,0,0} - v_{los,c,0,0}\right)T_p n \\ +\frac{4\gamma_{T,0}}{c^2}\left(r_{s,0,0} - r_{c,0,0}\right)\left(v_{los,s,0,0} - v_{los,c,0,0}\right)T_p n \\ +\frac{2\gamma_{T,0}}{c^2}\left(v_{los,s,0,0} - v_{los,c,0,0}\right)^2\left(T_p n\right)^2 \\ -\frac{2}{c}\gamma_{T,0}\left(1-\zeta_n\right)\left(v_{los,s,0,0} - v_{los,c,0,0}\right)T_p n T_s i \end{array} \right) \right\} \quad \text{(A50)}$$

or

$$X_V(i,n) = A_r \exp\left\{ j \left(\begin{array}{l} -\frac{2\omega_{T,0}}{c}\left(r_{s,0,0} - r_{c,0,0}\right) + \frac{2\gamma_{T,0}}{c^2}\left(r_{s,0,0} - r_{c,0,0}\right)^2 \\ -\frac{2\gamma_{T,0}}{c}\left(\zeta_0 - \zeta_n\right)\left(r_{s,0,0} - r_{c,0,0}\right) T_s i \\ -\frac{2}{c}\gamma_{T,0}\left(1-\zeta_n\right)\left(v_{los,s,0,0} - v_{los,c,0,0}\right) T_p n T_s i \\ -\frac{2\gamma_{T,0}}{c}\left(1-\zeta_0\right)\left(r_{s,0,0} - r_{c,0,0}\right) T_s i \\ -\frac{2\omega_{T,0}}{c}\left(v_{los,s,0,0} - v_{los,c,0,0}\right) T_p n \\ +\frac{4\gamma_{T,0}}{c^2}\left(r_{s,0,0} - r_{c,0,0}\right)\left(v_{los,s,0,0} - v_{los,c,0,0}\right) T_p n \\ +\frac{2\gamma_{T,0}}{c^2}\left(v_{los,s,0,0} - v_{los,c,0,0}\right)^2 \left(T_p n\right)^2 \end{array} \right) \right\}. \qquad \text{(A51)}$$

We observe the following.

- The first line of the phase expression is constant. Therefore it does not contribute to ascertaining range or velocity of the target.
- The last line of the phase expression is quadratic in index *n*. While it may defocus the Doppler response, it does not contribute to its location.
- The second and third lines of the phase expression are a function of both indices *n* and *i*. They represent migration terms. They are typically ignored in coarse resolution GMTI systems.

Ignoring these terms allows us to simplify the video phase error expression to

$$X_V(i,n) = A_r \exp\left\{ j \left(\begin{array}{l} -\frac{2\gamma_{T,0}}{c}\left(1-\zeta_0\right)\left(r_{s,0,0} - r_{c,0,0}\right) T_s i \\ -\frac{2\omega_{T,0}}{c}\left(v_{los,s,0,0} - v_{los,c,0,0}\right) T_p n \\ +\frac{4\gamma_{T,0}}{c^2}\left(r_{s,0,0} - r_{c,0,0}\right)\left(v_{los,s,0,0} - v_{los,c,0,0}\right) T_p n \end{array} \right) \right\}. \qquad \text{(A52)}$$

Typically in simple GMTI, the first phase term is exploited to determine target range, and the second phase term is exploited to determine target Doppler, although the third term will perturb the answer somewhat. The third term is a result of the RVPE term previously discussed.

We identify the velocity difference as

$$\left(v_{los,s,0,0} - v_{los,c,0,0}\right) = \left(\frac{\mathbf{r}_s\left(t_0 + t_{c,0,0}\right)}{\left|\mathbf{r}_s\left(t_0 + t_{c,0,0}\right)\right|} - \frac{\mathbf{r}_c\left(t_0 + t_{c,0,0}\right)}{\left|\mathbf{r}_c\left(t_0 + t_{c,0,0}\right)\right|} \right) \bullet \mathbf{v}_c - v_{los,t,0,0} \qquad \text{(A53)}$$

where all values are instantaneous values at time corresponding to $n = 0$ and $i = 0$, that is for the central sample of the central pulse of the CPI.

Note that the dot product is merely the difference between line-of-sight velocities to the target location and the SRP.

Note also that the best we can extract from the data is the quantity $\left(v_{los,s,0,0} - v_{los,c,0,0}\right)$. This leaves a fundamental ambiguity in being unable to separate the target's own velocity from the velocity manifestation due to target location. Even if the target were stationary, there would be a velocity component due to its offset from the SRP. It is precisely this phenomenon that is exploited by SAR.

"Do not worry about your difficulties in Mathematics. I can assure you mine are still greater." -- Albert Einstein

Reference

[1] J. T. Cordaro, J. J. Mason, J. A. Hollowell, "Detection of Moving Targets Using Simultaneous Synthetic Aperture Radar (SAR) and Moving Target Indicator (MTI) Radar – LDRD Final report", Sandia Report SAND99-3125, Specified Dissemination, Export Controlled Information, December 1999.

[2] William J. Caputi, Jr., "Stretch: A Time-Transformation Technique", *IEEE Transactions on Aerospace and Electronic Systems*, Vol. AES-7, No. 2, pp 269-278, March 1971.

[3] J. L. Walker, "Range-Doppler Imaging of Rotating Objects," *IEEE Trans. on Aerospace and Electronic Systems*, AES-16 (1), pp 23-52, 1980.

[4] Armin W. Doerry, "Wavefront Curvature Limitations and Compensation to Polar Format Processing for Synthetic Aperture Radar Images", Sandia Report SAND2007-0046, Unlimited Release, January 2007.

[5] Merrill I. Skolnik, ed., *Radar Handbook*, McGraw-Hill, 1970.

[6] F. E. Nathanson, *Radar Design Principles*, second edition, ISBN 0-07-046052-3, McGraw-Hill, Inc., 1990.

Distribution

Unlimited Release

1	MS 1330	B. L. Burns	5340	
1	MS 0519	T. J. Mirabal	5341	
1	MS 1330	M. S. Murray	5342	
1	MS 1330	W. H. Hensley	5342	
1	MS 1330	S. D. Bensonhaver	5342	
1	MS 1330	T. P. Bielek	5342	
1	MS 1330	J. D. Bradley	5342	
1	MS 1330	A. W. Doerry	5342	
1	MS 1330	D. W. Harmony	5342	
1	MS 1330	J. A. Hollowell	5342	
1	MS 1330	C. Musgrove	5342	
1	MS 1330	S. Nance	5342	
1	MS 1332	R. Riley	5342	
1	MS 1330	J. A. Rohwer	5342	
1	MS 1330	B. G. Rush	5342	
1	MS 1330	G. J. Sander	5342	
1	MS 1330	D. G. Thompson	5342	
1	MS 0501	P. R. Klarer	5343	
1	MS 1330	K. W. Sorensen	5345	
1	MS 0529	B. C. Brock	5345	
1	MS 1330	D. F. Dubbert	5345	
1	MS 0529	G. K. Froehlich	5345	
1	MS 1330	F. E. Heard	5345	
1	MS 1330	G. R. Sloan	5345	
1	MS 1330	S. M. Becker	5348	
1	MS 1330	O. M. Jeromin	5348	
1	MS 1330	S. A. Hutchinson	5349	
1	MS 0519	D. L. Bickel	5354	
1	MS 0519	A. Martinez	5354	
1	MS 0899	Technical Library	9536	(electronic copy)

;-)